Numerical Simulation of Deep Tropical Convection Associated with Large-Scale Convergence

FRANK B. LIPPS AND RICHARD S. HEMLER

Geophysical Fluid Dynamics Laboratory/NOAA, Princeton University, Princeton, NJ 08542

(Manuscript received 18 April 1985, in final form 10 February 1986)

ABSTRACT

A set of four-hour simulations has been carried out to study deep moist convection characteristic of the Global Atmospheric Research Program (GARP) Atlantic Tropical Experiment (GATE). The present model includes warm rain bulk cloud physics and effects associated with a large-scale, time-invariant convergence. The convection took approximately two hours to develop from a random moisture disturbance. The cloud efficiency, in terms of the total water vapor condensed, was near 40%.

The heat and moisture budgets and the time-mean vertical fluxes of mass, heat, and moisture were calculated for the last 80 minutes of the simulations. In this study the primary emphasis was placed upon run A, the three-dimensional calculation. For this calculation, the layer centered near 4.0 km was a region of low mean cloudiness but of strong convection. The upward mass flux was strong and upward heat and moisture fluxes had maximum values in this layer. The strongest downward mass flux was due to weak downward velocities in the rainy area below cloud base.

Time-mean data were also calculated for vertical velocity cores and compared with observed data. In run A, virtually all updraft cores are in-cloud and for a deep layer between 2.5 and 8.0 km the in-cloud upward mass flux is nearly all associated with cores. In this layer the upward mass flux due to cores is approximately twice the mass flux associated with the large-scale convergence. The fractional area of updraft cores is small, varying between 2.5% and 4.0% for vertical levels between 1 and 11 km. Calculated values of core diameter $\bar{D}$ are in relatively good agreement with the observed data. For values of mean vertical velocity $\bar{w}$, however, the agreement is not nearly as good. For downdraft cores, values of $\bar{w}$ are significantly smaller than the observations. For updraft cores, values of $\bar{w}$ at lower levels are small, whereas values in the upper levels are in reasonable agreement with observations. The weak updraft cores at lower levels may be related to the absence of strong gust fronts in the present simulations.

1. Introduction

The onset of deep moist convection associated with large-scale tropical disturbances is an important problem which has been examined by several diagnostic studies. As in most of these studies, Ogura et al. (1979) have analyzed data for disturbances observed during the GARP[1] Atlantic Tropical Experiment (GATE). They found for all cases considered that low-level convergence and, therefore, upward motion was present or enhanced prior to the development of organized convective systems. The more recent study of Chen and Ogura (1982) observed a time lag of 5–10 hours between the maxima of surface convergence and the precipitation rate. These results are consistent with the earlier findings of Cho and Ogura (1974), Frank (1978) and Johnson (1978). Thus, in the numerical simulation of the associated small-scale convection, it appears necessary to have an adequate representation of large-scale convergence in the numerical model. This is especially relevant when time-mean statistics are to be calculated over a time period of one to several hours.

Two-dimensional numerical calculations for deep moist convection with realistic large-scale forcing have been carried out by Soong and Tao (1980). The data for the large-scale flow were obtained from the study of Ogura et al. (1979). An analysis of the large-scale forcing by Soong and Tao indicated that the dominant terms were due to vertical advection of moisture and potential temperature by the mean vertical velocity. As shown in their Fig. 7, the horizontal advection of moisture by the large-scale flow is a smaller, but non-negligible, effect.

In the present study, a set of four-hour numerical simulations is carried out with a large-scale, time-invariant convergence present. The purpose of these calculations is to examine the time-mean statistics and transient behavior for this type of deep moist convection. A longer-term goal is to use data from this and other studies to improve the cumulus parameterization for tropical convection in large-scale numerical models. Both two- and three-dimensional convection are simulated and the present results are compared with ob-

[1] Global Atmospheric Research Program.

servations and the model results of Soong and Tao (1980).

The base state potential temperature $\theta_0(z)$ and water vapor mixing ratio $q_v(z)$ are obtained from the same data as used by Soong and Tao. The profile of mean vertical velocity, calculated from the large-scale convergence, is likewise taken from this data set. Since their previous work indicated that the mean vertical velocity has the dominant role in the large-scale forcing, all other large-scale effects, such as those due to horizontal advection and radiation, have been neglected. The present study also does not include any effects due to vertical wind shear. For this reason the present calculations have the most relevance for tropical convection in which vertical wind shear is of minimum importance.

The moist convection numerical model is described in section 2. This discussion includes the form of model equations and boundary conditions as well as the numerical methods used. The effect of the time-invariant, large-scale convergence is represented by vertical advection terms in the thermodynamic and moisture equations. A detailed discussion of the subgrid-scale mixing processes and the warm rain bulk cloud physics is given in the Appendix.

The primary calculations and the initial base state are described in section 3. These computations are a set of four-hour simulations in which the initial disturbance is a random moisture distribution. For all these computations, periodic lateral boundary conditions are used. In the present study, the major emphasis will be placed on the first simulation, run A, which is the three-dimensional calculation. In section 4 the time-variation of the volume–mean kinetic energy and the cloud efficiency over the four hours are presented. Various time–mean statistics calculated over the last 80 minutes of the simulations are given in section 5. These include the variation of mean cloudiness and relative humidity with height, the temperature and moisture budgets, and vertical fluxes of mass, heat and moisture. In section 6 the distribution of updraft and downdraft vertical velocity cores on specific horizontal levels is calculated. These data are compared with the data obtained from observations by LeMone and Zipser (1980).

2. The moist convection model

The dynamical framework of the present model follows that given in the scale analysis of Lipps and Hemler (1982). As in the earlier study, the set of governing equations is anelastic (Ogura and Phillips, 1962) and Cartesian (x, y, z)-coordinates are used. The base state potential temperature $\theta_0(z)$ is a slowly varying function of z and the pressure p is represented through the Exner function

$$\pi = \left(\frac{p}{P}\right)^{\kappa}, \quad \kappa = R_d/c_p \tag{2.1}$$

where P (=1015 mb) is a reference pressure, R_d (=287.04 J kg^{-1} K^{-1}) is the gas constant and c_p (=1005.7 J kg^{-1} K^{-1}) the specific heat at constant pressure for dry air. Since θ_0 is a slowly varying function in the vertical, Lipps and Hemler (1982) show that the dynamic pressure term in the equations of motion can be represented by the gradient of the scalar ϕ. The variable ϕ is given by

$$\phi = c_p\theta_0\pi_1 \tag{2.2}$$

where π_1 is the first-order term in the expansion of π [see Eq. (2.5)].

In the present model the saturation water vapor mixing ratio q_{vs} is given by

$$q_{vs} = \frac{\epsilon e_s}{p_0 - e_s} \tag{2.3}$$

where $p_0(z)$ is the base state pressure, e_s the saturation vapor pressure, $\epsilon = R_d/R_v$, and R_v (=461.50 J kg^{-1} K^{-1}) the gas constant for water vapor. This form of q_{vs} is more accurate than often used as it includes the term $-e_s$ in the denominator. It was found in run C of Lipps and Hemler (1982) that inclusion of this term resulted in larger values of q_{vs} which gave rise to significantly reduced condensation and less vigorous convection.

An important feature of the present model is that a large-scale, time-invariant convergence associated with the synoptic flow is assumed to exist. The magnitude of this convergence is of the order of 10^{-5} s^{-1}. Thus the convergent flow is sufficiently weak to be negligible in the development of isolated moist convective cells. For dynamical effects which occur on a longer time scale, however, the convergence is important. Therefore, the convergence will play an important role in the time evolution of the horizontal average potential temperature and moisture fields. In this model there is no feedback mechanism between the strength of the convection and the strength of the convergence. A similar approach has been used in several previous studies; e.g., Sommeria (1976), Chen and Orville (1980), Soong and Tao (1980, 1984) and Soong and Ogura (1980).

In discussing the role of convergence, we let the scalar s represent either the potential temperature or the moisture field. Denoting the horizontal average by $\langle s \rangle$, we assume that the convergent flow velocities (U, V, W) interact only with $\langle s \rangle$. Thus it is seen that the total advection of $\langle s \rangle$ due to (U, V, W) is given by

$$\text{advection } (\langle s \rangle) = \rho_0 W \frac{\partial}{\partial z}(\langle s \rangle) \tag{2.4}$$

where ρ_0 is the base state density. Vertical advection terms as given in (2.4) are included in the potential temperature and water vapor mixing ratio equations discussed in section 2b. In all other equations the effect of the mean convergence is assumed to be negligible.

a. Expansion of the thermodynamic variables

For the present set of anelastic equations the potential temperature θ, the temperature T, and the pressure function π can be written as

$$\left.\begin{aligned}\theta &= \theta_0(z) + \theta_1(x, y, z, t)\\ T &= T_0(z) + T_1(x, y, z, t)\\ \pi &= \pi_0(z) + \pi_1(x, y, z, t)\end{aligned}\right\} \quad (2.5)$$

where θ_0, T_0 and π_0 represent the base state and θ_1, T_1 and π_1 represent the effects of the deep moist convection. The definition of θ implies the relation $T = \pi\theta$. Since the dynamic pressure can be neglected to first order (Wilhelmson and Ogura, 1972; Lipps and Hemler, 1982), this relation can be split into the two components

$$T_0 = \pi_0\theta_0, \quad T_1 = \pi_0\theta_1. \quad (2.6)$$

The base state is hydrostatic so that

$$0 = -c_p\theta_0 \frac{d\pi_0}{dz} - g \quad (2.7a)$$

where g (=9.781 m s^{-2}) is the acceleration due to gravity. Using the relation $T_0 = \pi_0\theta_0$, we note that the above equation can be put in the form

$$\frac{d \ln \pi_0}{dz} = -\frac{g}{c_p T_0}. \quad (2.7b)$$

The reference pressure P in (2.1) is chosen such that $\pi_0 = 1$ at $z = 0$. Thus, knowing $T_0(z)$ from observed data, $\pi_0(z)$ can be calculated from (2.7b) and $\theta_0(z)$ can be obtained from $T_0 = \pi_0\theta_0$.

b. The equations of motion

The equations describing the deep convection are written in flux form using tensor notation. The anelastic equation for mass continuity is

$$\frac{\partial}{\partial x_j}(\rho_0 u_j) = 0. \quad (2.8)$$

Since θ_1, T_1 and π_1 represent small deviations from their base state counterparts, the momentum equation for the moist air is given by

$$\frac{\partial}{\partial t}(\rho_0 u_i) + \frac{\partial}{\partial x_j}(\rho_0 u_i u_j) = -\rho_0 \frac{\partial \phi}{\partial x_i} + \delta_{i3}\rho_0 g \times \left(\frac{\theta_1}{\theta_0} + 0.608 q_v - q_c - q_r\right) + \frac{\partial \tau_{ij}}{\partial x_j} \quad (2.9)$$

where the vector velocity (u, v, w) is represented by u_i, ϕ is defined in (2.2), τ_{ij} is the subgrid-scale Reynolds stress tensor, and q_v, q_c, and q_r are the mixing ratios of water vapor, cloud water and rain water. The constant 0.608 is equal to $(R_v/R_d) - 1$, and δ_{ij} represents the Kronecker delta function. Since the present set of equations is anelastic, the variable ϕ is calculated from a Poisson equation which is obtained by taking the divergence of Eq. (2.9).

The thermodynamic equation and the equations governing moisture conservation are

$$\frac{\partial}{\partial t}(\rho_0\theta_1) + \frac{\partial}{\partial x_j}[\rho_0 u_j(\theta_0 + \theta_1 - \theta_{00})] = \frac{\rho_0 L}{c_p \pi_0}(C_d - E) - W\frac{\partial}{\partial z}\langle\theta_0 + \theta_1\rangle - \frac{\partial}{\partial x_j}(\rho_0\overline{u_j'\theta'}) \quad (2.10)$$

$$\frac{\partial}{\partial t}(\rho_0 q_v) + \frac{\partial}{\partial x_j}(\rho_0 u_j q_v) = -\rho_0(C_d - E) - W\frac{\partial\langle q_v\rangle}{\partial z} - \frac{\partial}{\partial x_j}(\rho_0\overline{u_j' q_v'}) \quad (2.11)$$

$$\frac{\partial}{\partial t}(\rho_0 q_c) + \frac{\partial}{\partial x_j}(\rho_0 u_j q_c) = \rho_0(C_d - S_a - S_c) - \frac{\partial}{\partial x_j}(\rho_0\overline{u_j' q_c'}) \quad (2.12)$$

$$\frac{\partial}{\partial t}(\rho_0 q_r) + \frac{\partial}{\partial x_j}(\rho_0 u_j q_r) - \frac{\partial}{\partial z}(\rho_0 V_T q_r) = \rho_0(S_a + S_c - E) - \frac{\partial}{\partial x_j}(\rho_0\overline{u_j' q_r'}) \quad (2.13)$$

where $\rho_0\overline{u_j'\theta'}$, $\rho_0\overline{u_j' q_v'}$, $\rho_0\overline{u_j' q_c'}$ and $\rho_0\overline{u_j' q_r'}$ are the subgrid-scale fluxes associated with θ, q_v, q_c and q_r. Expressions for these subgrid-scale quantities as well as τ_{ij} are given in the Appendix. The present formulation of subgrid-scale mixing is similar to that in Lipps and Hemler (1982). The primary difference is that in the present model in regions of stable stratification outside of clouds the vertical mixing is greatly reduced.

The terms involving W in (2.10) and (2.11) are associated with the large-scale convergence [see discussion of Eq. (2.4)]; L (=0.2501 × 10^7 J kg^{-1}) is the latent heat of vaporization and θ_{00} (=339.4 K) is a constant included in (2.10) to improve the accuracy of the numerical integration.

Following Kessler (1969) the ice-phase is omitted and liquid water is separated into cloud water q_c which moves with the air and rain water q_r which falls relative to the air with the fall velocity $-V_T$. The remaining quantities in (2.10)–(2.13) are the condensation/evaporation C_d of cloud water q_c, the evaporation E of rain water q_r and the total conversion $(S_a + S_c)$ of q_c into q_r. Detailed expressions for S_a, S_c, V_T and E are also given in the Appendix. The present warm rain bulk cloud physics is a modified version of that discussed by Manton and Cotton (1977).

The values of C_d are determined by requiring $q_v = q_{vs}$ whenever cloud water q_c is present. The method of calculation of C_d follows that given in appendix A of Lipps and Hemler (1982). Note that, as indicated earlier, the saturation water vapor mixing ratio q_{vs} is specified by (2.3).

c. Numerical methods

Equations (2.8)–(2.13) represent a complete set of equations for the variables u_i, ϕ, θ_1, q_v, q_c and q_r subject to the appropriate boundary conditions. These are discussed in the next section. As previously stated, ϕ is obtained from the solution of a Poisson equation. Grid points for u, v, w and ϕ are staggered in space with the Poisson equation for ϕ being solved at ϕ-grid points (Harlow and Welch, 1965; Williams, 1969). The variables θ, q_v, q_c and q_r are also evaluated at ϕ-grid points. The details of the solution of the Poisson equation follow that discussed by Williams (1969).

The momentum equation (2.9) is solved using centered time and space differences as in Lipps and Hemler (1982). This finite difference method is momentum and kinetic energy conserving with respect to the nonlinear advective terms (Piacsek and Williams, 1970). The prognostic equations (2.11)–(2.13) for q_v, q_c and q_r are solved using the method given by Clark (1979). This method involves a hybrid finite difference scheme based on a second order in space and first order in time Crowley (1968) scheme and an upstream differencing scheme which is first order in both space and time. The motivation for using this scheme is to eliminate the problem of numerically generated spurious negative values of q_v, q_c and q_r. The possibility of spurious negative values is most relevant for q_c and q_r. As discussed by Clark (1979), away from regions where such values are likely, the present numerical method is very close to the unmodified Crowley scheme.

The prognostic equation (2.10) for θ_1 is solved by using the second-order Crowley (1968) scheme. This method of solution of (2.10) is consistent with the solution of (2.11) for q_v and thus allows an efficient numerical algorithm for calculating the condensation/evaporation C_d of cloud water. The nonlinear terms in the Crowley and modified Crowley schemes conserve the linear variables θ_1, q_v, q_c and q_r. Quadratic forms, however, are not conserved. In spite of this deficiency, Mahlman and Sinclair (1977) indicate that the numerical errors associated with the second-order Crowley scheme are roughly equivalent with those associated with second-order linear and quadratic conserving schemes.

d. Boundary conditions

Periodicity is required at the lateral side boundaries as in previous studies (Lipps and Hemler, 1982; Lipps, 1977). In all numerical calculations the model domain is 16 km deep and the vertical grid interval $\Delta z = 250$ m. At $z = 0$ and $z = 16$ km rigid boundaries are assumed so that $w = 0$ there. Due to the staggered grid used in the present model, the variables u, v, θ, q_v, q_c and q_r are evaluated at a one-half grid interval (125 m) from the upper boundary. At this level the vertical finite difference derivatives of $\rho_0\overline{w'u'}$, $\rho_0\overline{w'v'}$, $\rho_0\overline{w'\theta'}$, $\rho_0\overline{w'q_v'}$, $\rho_0\overline{w'q_c'}$, $\rho_0\overline{w'q_r'}$ are required to vanish as in Klemp and Wilhelmson (1978). These conditions minimize unrealistic subgrid-scale viscous and diffusive effects near the upper boundary. It should be noted that in terms of the Reynolds stress τ_{ij} in (2.9) we have $\tau_{13} = -\rho_0\overline{w'u'}$ and $\tau_{23} = -\rho_0\overline{w'v'}$.

Before discussing the remaining surface boundary conditions, we note that the model coordinate system is required to translate at a speed of 2.4 m s^{-1} toward the north-northwest. This speed was obtained from an inspection of Fig. 4 of Soong and Tao (1980) for 12 August 1974, the date chosen for the present numerical simulations. It represents the mean value of the wind speed in the lower and middle troposphere as shown by their data. In the present model the positive x-axis is directed south-southeast so that this translation is represented by a velocity of -2.4 m s^{-1} parallel to the x-axis.

At the surface, located at $z = 0$, the vertical derivatives of q_c and q_r are required to vanish and a drag law formulation is used to specify $\rho_0\overline{w'u'}$, $\rho_0\overline{w'v'}$, $\rho_0\overline{w'\theta'}$, $\rho_0\overline{w'q_v'}$. This formulation is similar to that used by Soong and Ogura (1980) for heat and moisture fluxes. The drag coefficient is given by Roll (1965) as

$$C_D = (1.10 + 0.04V) \times 10^{-3} \tag{2.14}$$

where V is the total horizontal wind speed with respect to the earth's surface and defined as

$$V = [(u - 2.4)^2 + v^2]^{1/2}. \tag{2.15}$$

The drag law relations are given by

$$\rho_0(\overline{w'u'})_{\text{sfc}} = -\rho_0 C_D V(u - 2.4) \tag{2.16}$$

$$\rho_0(\overline{w'v'})_{\text{sfc}} = -\rho_0 C_D V v \tag{2.17}$$

$$\rho_0(\overline{w'\theta'})_{\text{sfc}} = -\rho_0 C_D V(\theta - \theta_{\text{sfc}}) \tag{2.18}$$

$$\rho_0(\overline{w'q_v'})_{\text{sfc}} = -\rho_0 C_D V[q_v - (q_v)_{\text{sfc}}] \tag{2.19}$$

where the subscript "sfc" refers to surface values and the nonsubscripted variables V, u, v, θ and q_v are evaluated at the lowest grid level ($z = 125$ m). The value of θ_{sfc} is 27.4°C and $(q_v)_{\text{sfc}} = 2.33 \times 10^{-2}$, which is the saturation value of q_v for the temperature of 27.4°C.

In some earlier runs, intense gravity waves developed in the upper levels, presumably caused by reflection at the upper rigid boundary ($z = 16$ km) and by trapping in the horizontal due to the periodic boundary conditions. In order to remove these waves, a Newtonian damping term was added to the right side of Eq. (2.10) for $z \geqslant 13.875$ km. This damping term is given by

$$\frac{\partial}{\partial t}(\rho_0\theta_1)|_{\text{damping}} = -0.5 \times 10^{-6}(z - z_0)(\theta_1 - \langle\theta_1\rangle) \tag{2.20}$$

where $z_0 = 13.875$ km. Thus the magnitude of the damping linearly increases as z increases from $z = z_0$ to $z = 16$ km. With $z - z_0$ given in meters, (2.20) implies a damping constant of about 6.5 minutes near $z = 15$ km.

3. Set of calculations and the initial base state

In this study, a set of four-hour numerical simulations is carried out for deep maritime tropical convection with a large-scale, time-invariant convergence present. The model used for these calculations is described in section 2. The initial base state sounding of potential temperature θ_0 and relative humidity RH is shown in Fig. 1. These curves are obtained as smoothed profiles of the data given in Fig. 6 of Soong and Tao (1980). Thus, Fig. 1 represents a smoothed version of the vertical sounding taken from the ship *Researcher* at 0600 GMT 12 August 1974 in the GATE region. The curve labeled θ_{moist} is the result of a pseudo-moist-adiabatic parcel calculation with cloud base at the same temperature as the environment at $z = 625$ m. This parcel calculation is carried out as described in Lipps and Hemler (1980). Note the close proximity of the θ_0 and θ_{moist} curves below $z = 3$ km in Fig. 1. Thus, the present sounding has weak moist instability for these lower levels.

The profile of vertical velocity W associated with the large-scale convergence is shown in Fig. 2. This curve is also obtained from Soong and Tao (1980), being a smoothed profile of the data shown in their Fig. 3 for 0600 GMT.

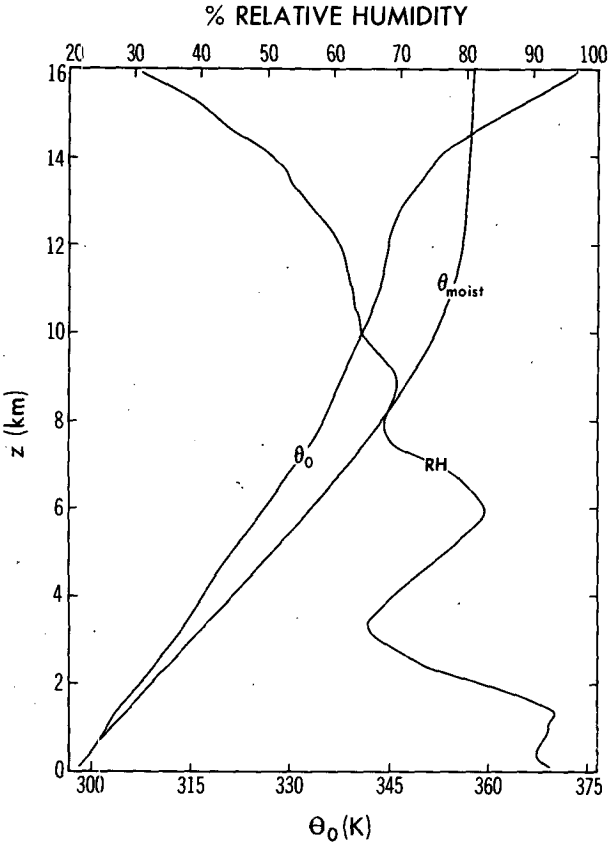

FIG. 1. The initial base state sounding of potential temperature $\theta_0(z)$ and of relative humidity RH(z) for the present calculations. The profile of θ_{moist} is obtained from a parcel calculation.

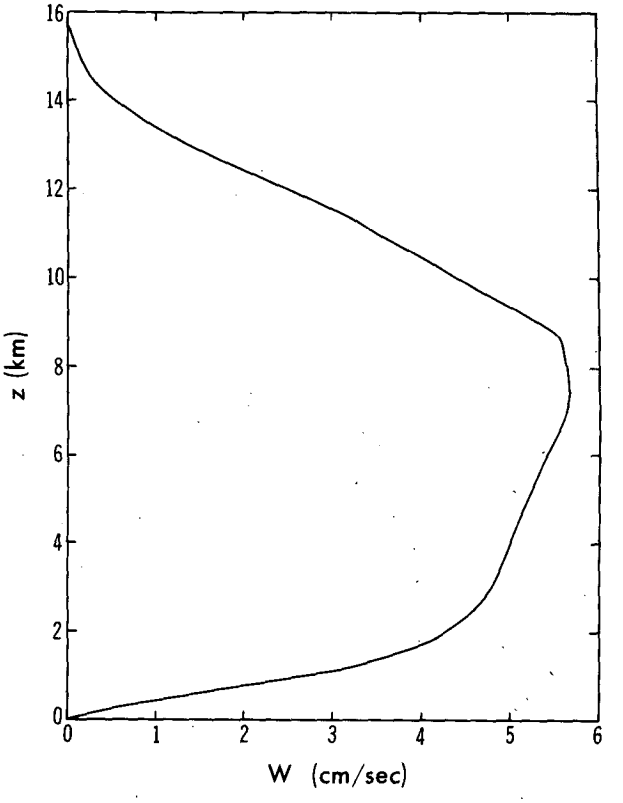

FIG. 2. Profile of vertical velocity W associated with the large-scale convergence.

Four-hour numerical simulations have been carried out for both two- and three-dimensional convection. In all calculations the vertical depth of the model is 16 km and the grid intervals are $\Delta z = 250$ m and $\Delta x = \Delta y = 500$ m. A summary of the primary calculations A–C is given in Table 1. The three-dimensional calculation, run A, has a horizontal domain of 24 km in x and 16 km in y. For the two-dimensional calculations, run B has the horizontal length of 32 km, whereas run C has the horizontal length of 64 km. As indicated in section 2, periodicity is required at the lateral side boundaries.

TABLE 1. Summary of primary calculations A–C. (IM and JM refer to the number of grid points in x and y. Also shown are the maximum values of vertical velocity w and disturbance potential temperature θ'_1, the time–mean, volume–average kinetic energy $\bar{K}$ and the horizontal-average rain at the ground R.)

Run	IM	JM	w (m s^{-1})	θ'_1 (K)	$\bar{K}$ (J m^{-3})	R (cm)
A	48	32	19.6	3.7	0.12	0.42
B	64	—	12.1	4.4	0.21	0.44
C	128	—	18.1	5.8	0.32	0.45

It is important to note that the present calculations are carried out with no vertical wind shear. The effects of wind shear on the convection, as well as the vertical transfer of momentum due to convection, are left as topics for future investigation.

4. Discussion of four-hour simulations

a. Time variation of kinetic energy

An important parameter describing the time evolution of the moist convection is the volume-mean kinetic energy K, which is defined by

$$K = \frac{1}{d}\int_0^d \rho_0 \frac{1}{2}\langle(u^2 + v^2 + w^2)\rangle dz \qquad (4.1)$$

where the angle brackets again indicate a horizontal average. The time variation of K for runs A–C is shown in Fig. 3.

In all calculations the convection was initiated by a random moisture disturbance applied at $t = 0$ in the lower levels ($0 < z \leqslant 875$ m). This disturbance is required to have a zero horizontal average at each vertical level and has a maximum amplitude of 2 g kg^{-1}. As seen in Fig. 3 the deep convection requires a long time to develop (at least 100 min for two-dimensional disturbances and 135 min for three-dimensional convection). Because it was considered possible that this long time for convection to form might be an artificial feature of the numerical model, the initial moisture disturbance was again applied at $t = 32$ min. This time was chosen as it is close to the time of minimum K with the initial forcing only. Adding the second forcing at $t = 32$ min results in a somewhat more rapid development of deep convection. The data shown in Fig. 3 have both the initial forcing at $t = 0$ and the second forcing at $t = 32$ min.

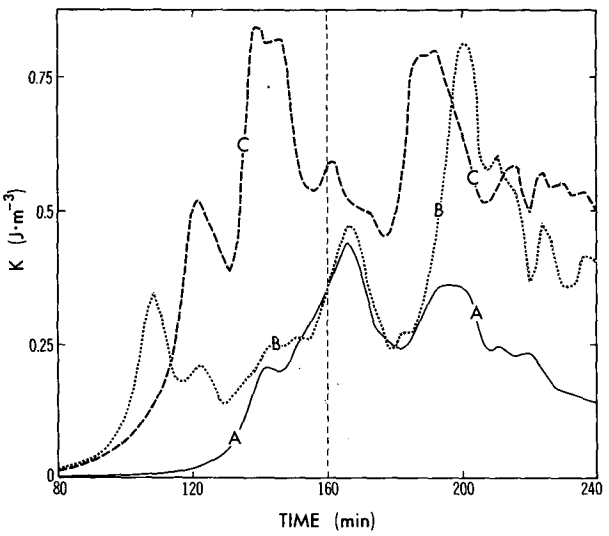

FIG. 3. Time variation of volume-mean kinetic energy K for runs A–C. Vertical dashed line at $t = 160$ min indicates start of 160–240 min region over which time-average data are calculated in section 5.

The authors now consider the long development time for deep convection to be a realistic result associated with the weak moist instability and relatively dry air in the lower levels as shown in Fig. 1. Zipser et al. (1981) in the discussion of their Fig. 13 suggest that a vertical lifting of 200 m in the lowest few kilometers is necessary before deep convection can develop in the observed rainband. The long start-up times shown in Fig. 3 are compatible with a vertical lifting of 200 m associated with the large-scale vertical velocity W shown in Fig. 2. Thus the present results appear to be in at least qualitative agreement with observations.

On comparing the time variation of K for runs A–C, one sees from Fig. 3 that the two-dimensional runs B and C develop deep convection earlier and have larger values of K throughout the simulations than the three-dimensional run A. This effect is also shown in the values of time-mean kinetic energy $\bar{K}$ given in Table 1. The reason for this result is not clear, but it suggests that in the present model the deep convection develops more easily and more often in the two-dimensional calculations. This suggestion is supported by the data in section 6 where vertical velocity cores (LeMone and Zipser, 1980) are discussed. It is found that the average area encompassed by both upward and downward cores is larger in runs B and C than in run A. (See Fig. 14.)

When comparing runs B and C, one sees that the values of K are larger in run C. From a look at the data in run C it is seen that, due to the longer horizontal domain, more intense disturbances form over a smaller fraction of the horizontal area than in run B. The more intense nature of the convection can be seen in Table 1 where the values of maximum vertical velocity w and disturbance potential temperature θ'_1 are larger for run C than for run B. Likewise, the time-mean $\bar{K}$ is larger for run C.

The final column in Table 1 shows the horizontal-average rain R at the ground at the end of four hours. In contrast to the other data in this table, the values of R are nearly insensitive to the dimensionality of the convection or the length of the horizontal domain in runs B and C. Thus the value of R is primarily determined by the large-scale convergence of moisture associated with the vertical velocity W.

b. Transient and time-mean convection for run A

Deep convection cells develop after two hours in run A as indicated by Fig. 3. These cells tend to be distributed in a random fashion throughout the horizontal domain. Clouds start developing at about 600 m above the surface and cloud tops reach slightly above 12 km. At the surface an average shower lasts about 40 minutes and gives approximately 4.0 cm of rainfall at its center. An interesting feature of cloud development is that near the time of maximum rainfall rate

the cloud base is usually near 4.0 km: downdrafts and heavy rain are below this level and cloud water and strong upward vertical velocity are above. New cells do form associated with outflow gust fronts at the surface, although these gust fronts are weaker than those observed in GATE. This aspect of the simulated convection is discussed in section 6.

A significant characteristic of the three-dimensional convection in run A is that definable patterns are seen when a combined vertical-time average is taken over the last two hours of this calculation. The horizontal patterns of the data thus averaged are shown in Fig. 4 for w, θ'_1, q_c and q_r. The correspondence between the various fields is clearly observed in this figure. A primary reason why individual cells stand out is that no mean wind is present relative to the numerical coordinate system. Thus individual cells tend to remain stationary in the horizontal during their life cycles so that definitive mean patterns are seen.

The relatively isolated nature of the strong cells is seen in Fig. 4a for the w-field. The heavy line represents the zero contour. Since $\langle w \rangle = 0$, it is evident that the area between the cells is made up of weakly descending w. The average size of a cell appears to be roughly (2.5 km)^2. A more accurate measure of the size of the strong convective cells, however, can be obtained from the data for vertical velocity cores discussed in section 6. It will be seen there that the diameter of strong updraft cores increases with height, being approximately 1.5 km in lower levels and 2.5 km in upper levels. The isolated nature of the strong cells is probably related to the lack of vertical wind shear in the present investigation. In the three-dimensional calculations of Tao (1983) with the observed wind shear included, initially randomly distributed clouds eventually became organized to form a line structure.

A property of the present averaging procedure is that the maximum values of w, θ'_1, q_c and q_r in Figs. 4a–d are roughly one-twentieth the size of the maximum values in the simulation. In Fig. 4c it should be noted that background cloudiness exists with the minimum value of $q_c = 3 \times 10^{-3}$ g kg^{-1}. This cloudiness occurs due to a high stratus layer centered at 6.5 km which forms early in the simulation due to the mean convergence. Later, when active cells are present, this stratus layer tends to break up due to downward motion between cells.

c. *Cloud efficiency*

In the present discussion cloud efficiency is defined as the total rain reaching the ground divided by the total positive cloud condensation occurring over a specific time interval. When expressed as a percentage, this value is multiplied by 100. The cloud efficiency diagram for the four-hour simulation in run A is shown

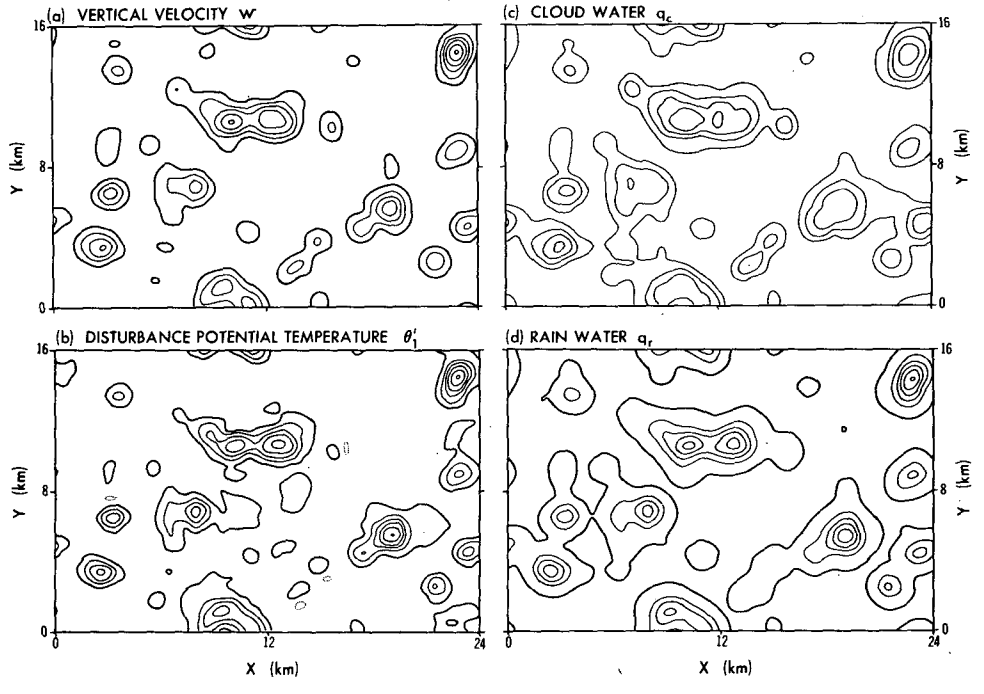

FIG. 4. Horizontal cross sections of variables averaged over z and over 2–4 h in run A. Time-averages obtained using data at 8 min intervals. Five contour intervals exist between zero contour (heavy) and the maximum value for each field. (a) Vertical velocity w, (b) disturbance potential temperature θ'_1, (c) cloud water q_c and (d) rain water q_r. The maximum values for w, θ'_1, q_c, and q_r are respectively 0.79 m s^{-1}, 0.19 K, 0.16 g kg^{-1} and 0.58 g kg^{-1}.

in Fig. 5. The values in the different boxes are normalized by the total positive cloud condensation CC integrated over the entire volume for the full four hours. Thus CE, RE and RAIN are normalized values of the total cloud water evaporation, rain water evaporation and total rain at the ground; ΔQC and ΔQR represent residual amounts of cloud water q_c and rain water q_r which were present at the end of four hours. By mass continuity of water substance we must have

$$1.00 = \text{CE} + \text{RE} + \Delta\text{QC} + \Delta\text{QR} + \text{RAIN}; \quad (4.2)$$

$S_a + S_c$ is the total conversion of cloud water into rain water and, again, by mass continuity we obtain

$$S_a + S_c = 1.00 - (\text{CE} + \Delta\text{QC}). \quad (4.3)$$

Similar data for the four simulations (runs A–D) are shown in Table 2. Run D is a calculation similar to run B except for a change in the bulk cloud physics. This run is discussed in more detail below.

The data in Table 2 indicate that the cloud efficiency E is approximately 40% for the primary calculations A–C. In run A the cloud efficiency is 5% larger than in the two-dimensional calculations B and C. This difference is associated primarily with the cloud water

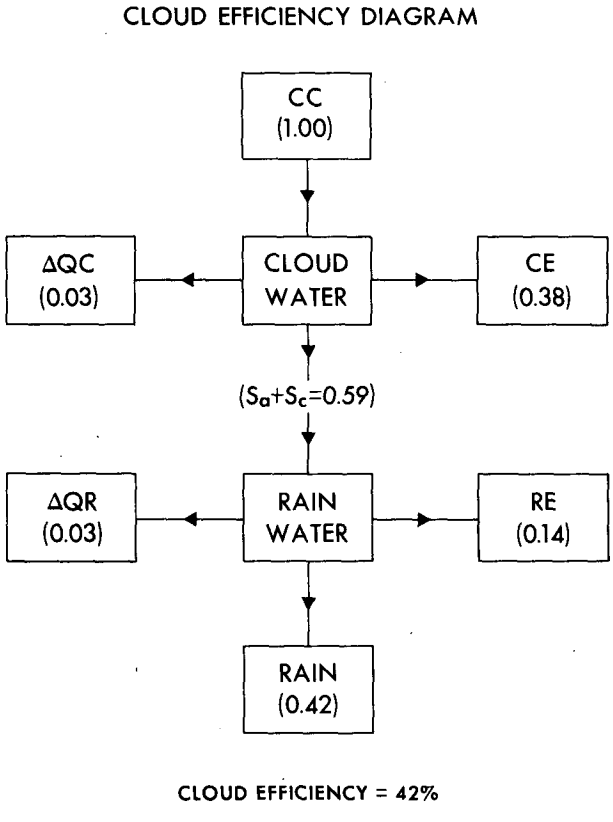

FIG. 5. Cloud efficiency diagram for run A. This figure corresponds to Eqs. (4.2) and (4.3). Data are averaged over the full 4 h. Values in each box are normalized by the total cloud condensation CC. For definitions of quantities in boxes see text.

TABLE 2. Summary of cloud efficiency data for the full 4 h simulations A–D. (Definitions of the various quantities tabulated are given in the text.)

Run	CE	RE	$S_a + S_c$	RAIN	ΔQC	ΔQR	E (%)
A	0.38	0.14	0.59	0.42	0.03	0.03	42
B	0.43	0.13	0.53	0.37	0.04	0.03	37
C	0.41	0.14	0.55	0.37	0.04	0.04	37
D	0.45	0.13	0.51	0.36	0.04	0.02	36

evaporation CE, which is 3%–5% larger in runs B and C than in run A. As is well known, the downward motion is relatively stronger in two-dimensional versus axisymmetric convection (Soong and Ogura, 1973; and others). In section 6 is will be seen that downward velocity cores are stronger in the two-dimensional simulations than in run A. Since downward motion associated with clouds leads to evaporation, this factor may explain the larger values of CE in two-dimensional convection and the resulting lower values of E.

Weisman and Klemp (1982) discuss precipitation efficiency in their study of the dependence of deep moist convection upon wind shear and buoyancy. It appears that their definition of precipitation efficiency is the same as that of cloud efficiency in the present study. For the cases of weak or no wind shear, the precipitation efficiencies shown in their Fig. 12 are comparable to the values of cloud efficiency in the present investigation.

Cloud efficiency was also discussed by Murray and Koenig (1972) who found a strong dependence on the form of warm rain bulk cloud physics (see their Fig. 9). In order to determine whether the exact form of cloud physics is important for our calculations, the onset value of $\rho_0 q_c \geq 0.42$ g m^{-3} for autoconversion S_a was increased to 1.5 g m^{-3} for the two-dimensional calculation run D. The data in Table 2 indicate only a slightly smaller value of E and a corresponding slightly larger value of CE than in run B. Thus the present values of E appear to be relatively insensitive to the exact form of warm rain bulk cloud physics. Left unanswered, however, is the importance of the ice phase which has been omitted from the present model.

5. Time-averaged data for the last 80 minutes

In order to determine some of the salient features while deep moist convection is active, it was decided to calculate the time-mean statistics for the last 80 minutes of runs A and B. The vertical dashed line at 160 min in Fig. 3 shows the start of the time-averaging interval between 160 and 240 min. This time interval appears to contain a representative range of convective activity after the initial startup of the deep convection. A longer time average would be desirable; however, it was not considered feasible to integrate the three-dimensional calculation, run A, significantly longer than

four hours. In the present study the primary discussion will center on run A.

The vertical profile of the time–mean, horizontal-average potential temperature $\langle\bar{\theta}\rangle$ for the last 80 minutes of run A is very similar to the profile of $\theta_0(z)$ shown in Fig. 1. The most significant difference between the profile of $\langle\bar{\theta}\rangle$ (not shown) and that of θ_0 is that the values of $\langle\bar{\theta}\rangle$ are uniformly cooler than those of θ_0. The average cooling of $\langle\bar{\theta}\rangle$ is approximately 1.0 K. The corresponding profile of time–mean, horizontal-average relative humidity RH is shown in Fig. 6a. Compared with the initial profile of RH in Fig. 1, it is seen that the relative humidity has significantly increased, especially in the upper levels. This cooler, more moist sounding over the last 80 minutes of run A is consistent with the vertical lifting required to initiate the convection as discussed in section 4a.

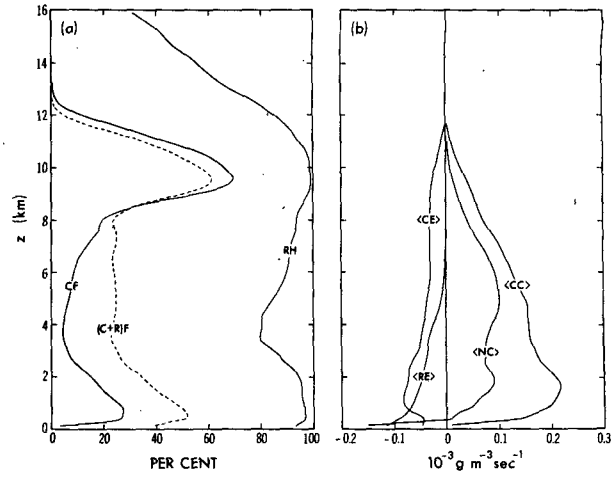

FIG. 6. Vertical variation of mean cloud properties for the last 80 min of run A. (a) Vertical distribution of the cloud fraction CF, cloud plus rain fraction $(C + R)F$ and the relative humidity RH. (b) Vertical distribution of the horizontal-average cloud water condensation $\langle CC\rangle$, cloud water evaporation $\langle CE\rangle$, rain water evaporation $\langle RE\rangle$ and net condensation $\langle NC\rangle$.

a. Variation of mean cloud properties

An important aspect of deep moist convection is the variation of average cloudiness with height and how this variation is related to the dynamics of the convection. Figure 6a also shows the time–mean horizontal-average cloud fraction CF and the cloud plus rain fraction $(C + R)F$ for the last 80 minutes of run A. It should be noted that the cloud fraction CF was determined by the criterion of whether any cloud water was present ($q_c > 0$). The curve for $(C + R)F$, however, was based on the criterion $q_c + q_r > 10^{-2}$ g kg^{-1} and was obtained from data at eight minute time intervals. The others curves in Fig. 6 were calculated using data at two minute intervals.[2] Comparing data for CF taken at eight minute and two minute intervals shows virtually identical results. Thus it is thought that the $(C + R)F$ curve calculated as an average from eight minute data is accurate.

In Fig. 6b are shown the vertical distribution of the horizontal-average cloud water condensation $\langle CC\rangle$, cloud water evaporation $\langle CE\rangle$, rain water evaporation $\langle RE\rangle$ and the net condensation $\langle NC\rangle$. The distributions $\langle CC\rangle$, $\langle CE\rangle$ and $\langle RE\rangle$ are formed as the product of the base state density ρ_0 and the horizontal average of the appropriate condensation/evaporation rate. By mass continuity $\langle NC\rangle$ is given by

$$\langle NC\rangle = \langle CC\rangle + \langle CE\rangle + \langle RE\rangle. \qquad (5.1)$$

Note that in the present discussion $\langle CE\rangle$ and $\langle RE\rangle$ are negative.

The vertical variation of the cloud fraction CF in Fig. 6a indicates a layer of maximum cloudiness near 10 km associated with high level outflow from deep convection. The secondary maximum in CF near 0.6 km is just above the planetary boundary layer and is associated with shallow convection. The layer between $z = 2.4$ km and $z = 6.4$ km has minimum cloudiness and corresponds to the layer of minimum relative humidity also shown in Fig. 6a. Even though the cloud fraction varies between 5% and 10% and the minimum relative humidity is 80% in this layer, it is a region of very active convection. As seen in Fig. 6b, the values of $\langle CC\rangle$ are large and $\langle NC\rangle$ has its maximum value in this layer. Also, as shown in Fig. 8, the in-cloud ($q_c > 0$) upward mass flux has a secondary maximum in this vertical region.

The dashed curve for the cloud plus rain fraction $(C + R)F$ shown in Fig. 6a has a minimum value of about 24% in midlevels and a maximum near 52% just above the boundary layer where CF is also large. It is of course expected that the curve for $(C + R)F$ would have larger values than the CF curve; however, as indicated by Lipps and Hemler (1982) there is likely to be some nonphysical horizontal diffusion of the rain water q_r by the numerical model. In the upper levels the values of $(C + R)F$ are less than those of CF. This is a result of some very diffuse clouds in the upper level outflow region and the use of the criterion $q_c > 0$ for the CF curve but $q_c + q_r > 10^{-2}$ g kg^{-1} for the $(C + R)F$ curve. It is acknowledged that the latter criterion to define the $(C + R)F$ curve is arbitrary. This criterion, however, does give a crude representation of the clouds and their immediate environment.

In Fig. 6b the maximum in $\langle CC\rangle$ and the lower level maximum in $\langle NC\rangle$ both occur near 1.8 km. Evidently these maxima are associated with the combined condensation effects due to deep and shallow convection. The curve for $\langle NC\rangle$ has a broad maximum near 4.75 km and is negative near the surface due to strong rain water evaporation $\langle RE\rangle$. As discussed below, these

[2] Unless noted in figure captions or the text, time averages in this study are obtained from data at two minute intervals.

effects play a dominant role in the temperature budget due to the resultant latent heat release. Near 10 km, where the high-level outflow is strong and CF is near 70%, cloud water evaporation $\langle CE \rangle$ nearly balances cloud water condensation $\langle CC \rangle$ so that $\langle NC \rangle$ is very small.

b. *Horizontal-average temperature and moisture budgets*

The horizontal-average, time-mean temperature and moisture budgets as a function of height are shown in Fig. 7 for the last 80 minutes of run A. These budgets are analogous to the data shown in Fig. 10 of Soong and Tao (1980) with the following differences: (i) Here the data are averaged over 80 minutes instead of 6 hours; (ii) a factor of ρ_0 is included in the present data and the height z represents the vertical; and (iii) the large-scale terms $\rho_0 S_\theta$ and $\rho_0 S_m$ include effects of vertical advection only. Thus $\rho_0 S_m$ does not include the horizontal advection of moisture, which is a significant term in Soong and Tao's study. The expressions for the large-scale cooling $\rho_0 S_\theta$ and moistening $\rho_0 S_m$ due to the mean vertical velocity W are given by

$$\rho_0 S_\theta = -\rho_0 \pi_0 W \frac{\partial \langle \bar{\theta} \rangle}{\partial z} \tag{5.2}$$

$$\rho_0 S_m = -\rho_0 W \frac{\partial \langle \bar{q}_v \rangle}{\partial z} \tag{5.3}$$

where the horizontal-average $\langle \bar{\theta} \rangle$ and $\langle \bar{q}_v \rangle$ are time-mean values over 80 minutes. It should be noted that the comparable components of $Q_1 - Q_R$ and $-(c_p/L)Q_2$ in Fig. 10 of Soong and Tao are calculated from observed data at 0600 GMT. This time represents the initial time, $t = 0$, in their study as well as here. Finally, their numerical calculations are two-dimensional whereas run A is a three-dimensinal simulation. Thus, while the present Fig. 7 can be compared with Fig. 10 of Soong and Tao, it should be remembered that there are significant differences in what the two figures represent.

In Fig. 7 the cloud heating effect $[\rho_0 \pi_0 (\partial \bar{\theta}/\partial t)_c]$ and the cloud moistening effect $[\rho_0 (\partial \bar{q}_v/\partial t)_c]$ represent the convective time tendencies due to all terms in the respective equations with the exception of the large-scale terms $\rho_0 S_\theta$ and $\rho_0 S_m$. Thus, when the curves for $-\rho_0 S_\theta$ and $-\rho_0 S_m$ are coincident with the respective cloud effect curves, there is no net heating or moistening at these horizontal levels during the 80 minute time average.

When examining the temperature budget in Fig. 7 the salient features are a strong net heating between 4

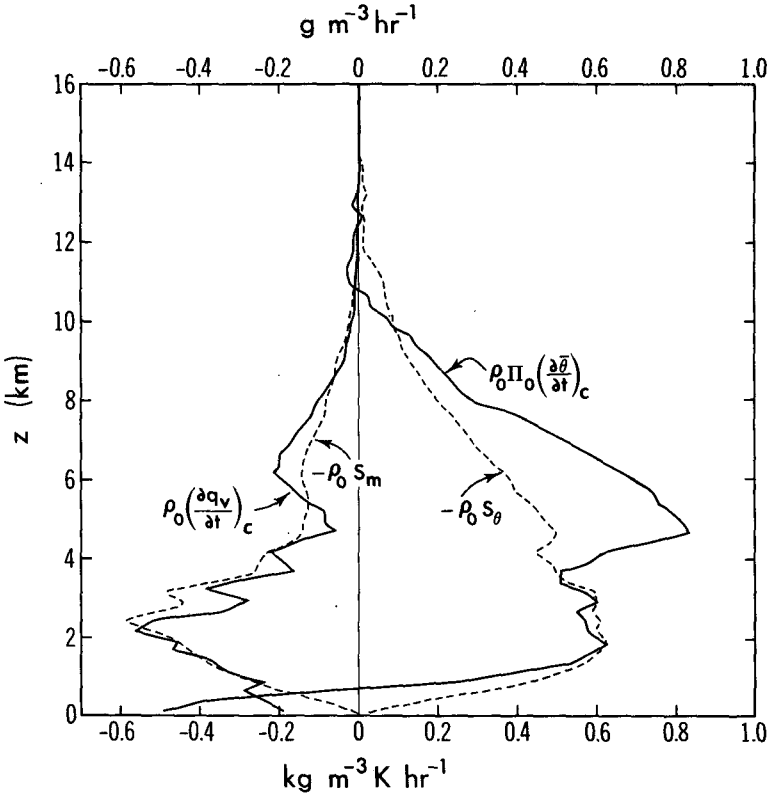

FIG. 7. The horizontal-average, time-mean temperature and moisture budgets as a function of height for the last 80 min of run A. The large-scale forcing terms $\rho_0 S_\theta$ and $\rho_0 S_m$ are defined by Eqs. (5.2) and (5.3).

and 8 km and a strong net cooling near the surface. Thus the atmosphere is being stabilized during this time period due to the convection. From Fig. 6b it is seen that 4–8 km are levels where the horizontal-average net cloud condensation $\langle NC \rangle$ is large and that $\langle NC \rangle$ is strongly negative near the surface due primarily to the large evaporation of rain water $\langle RE \rangle$. Thus the effects of change of phase and the resultant latent heating (or cooling) are dominant in the temperature budget. At 4.5 km the maximum in $[\rho_0 \pi_0 (\partial \bar{\theta}/\partial t)_c]$ is accentuated due to the cloud-scale vertical advection of temperature. Between approximately 1.5 and 3.5 km the cloud heating effect $[\rho_0 \pi_0 (\partial \bar{\theta}/\partial t)_c]$ and $-\rho_0 S_\theta$ are in near balance so that little net heating is occurring at these lower cloud levels. Above 10 km a weak net cooling exists, since the moist convection does not give rise to a sufficient warming to compensate for the adiabatic cooling associated with $\rho_0 S_\theta$.

The balance of terms for the moisture budget, shown on the left in Fig. 7, is not as simple as for the temperature budget. The cloud-scale vertical advection of moisture has a noisy pattern in the vertical and a larger relative amplitude than the cloud-scale vertical advection of temperature. Thus the cloud moistening effect $[\rho_0 (\partial \bar{q}_v/\partial t)_c]$ also has a noisy pattern in the vertical. Near the surface, downward flux of dry air dominates evaporation so that the $[\rho_0 (\partial \bar{q}_v/\partial t)_c]$ curve is more negative than the $-\rho_0 S_m$ curve. From 1 to 2 km the two curves are in near balance. Near 2 km, at the minimum of the $[\rho_0 (\partial \bar{q}_v/\partial t)_c]$ curve, the downward flux of dry air is nearly as large as the loss of moisture due to condensation. The small negative value of $[\rho_0 (\partial \bar{q}_v/\partial t)_c]$ at 4.7 km is associated with strong vertical advection of moisture, which nearly cancels the loss of moisture due to condensation. The secondary minimum of the $[\rho_0 (\partial \bar{q}_v/\partial t)_c]$ curve just above 6 km is due primarily to drying by condensation.

The temperature and moisture budgets were also calculated for the two-dimensional simulation run B and in many respects showed variations very similar to those indicated for run A in Fig. 7. When discussing the temperature budget, both runs A and B had a maximum net heating near 4.75 km associated with latent heat release and a net cooling near the surface due to evaporation of rain water. Likewise, for the moisture budget, both runs A and B had downward advection of dry air dominating evaporation near the surface and a maximum of upward advection of moist air near 4.7 km. Also, for both simulations, drying due to condensation dominated the large-scale curve $-\rho_0 S_m$ near 6 km.

c. *Vertical fluxes of mass, heat and moisture*

The upward and downward mass fluxes inside of the cloud plus rain area ($q_c + q_r > 10^{-2}$ g kg^{-1}) are shown by the solid curves labeled M_u and M_d in Fig. 8. The solid curve labeled M_e represents the net mass flux in the environment. In addition, the present figure has two short-dashed curves which represent the upward and downward mass fluxes in clouds only ($q_c > 0$). These mass fluxes are calculated from the total vertical velocity $w_t = w + W$, which is the sum of the cloud-scale and large-scale vertical velocities. The curves for M_u, M_d and M_e can be compared with the data of Soong and Tao (1980) shown in their Fig. 12. It should be noted that they use the criterion $q_c + q_r > 10^{-2}$ g kg^{-1} to define "in-cloud" in their study.

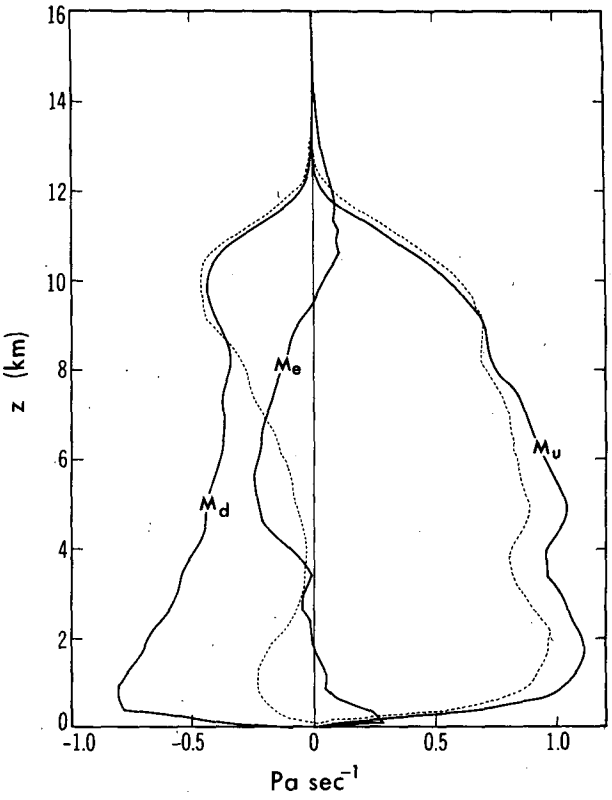

FIG. 8. The time-mean vertical mass flux for the last 80 min of run A: M_u, upward mass flux inside of clouds plus rain ($q_c + q_r > 10^{-2}$ g/kg); M_d, downward mass flux inside of clouds plus rain; M_e, net mass flux in the environment. The short-dashed curves represent upward and downward mass flux inside of clouds only ($q_c > 0$). Time averages obtained from data at 8 min intervals.

The curves for M_u and M_d in Fig. 8 indicate an approximate balance between upward and downward mass flux near cloud base (625 m). Above cloud base, the values of M_u are approximately double those of M_d until the region of high-level outflow is reached ($z \geq 10$ km) where M_u and M_d are roughly equivalent. Other noteworthy features of these curves are the double maxima in M_u and the strong minimum in M_d at cloud base. The profile for M_e indicates a significant downward mass flux for the middle layers (4–9 km) in the environment. Thus, forced subsidence due to the convection dominates the upward mass flux associated with W in these layers. In the upper levels M_e is positive, indicating the dominance of W over subsidence. Near the surface M_e is also positive, indicting forced vertical lifting outside the region of the precipitating downdrafts.

The curve for in-cloud ($q_c > 0$) upward mass flux indicates that, as expected, most of the upward mass flux occurs within the clouds. From $z = 0.5$ km to $z = 6.5$ km, the excess of the M_u mass flux over the in-cloud upward mass flux is relatively constant with height, being approximately 0.14 Pa s^{-1} or 12% of the total M_u mass flux. The curve for in-cloud downward mass flux has two minima; the stronger is associated with the high-level outflow region and the weaker with the shallow convection. The in-cloud downward mass flux due to shallow convection is quite weak, being much smaller in magnitude than the downward mass flux M_d. Thus it is seen that M_d is associated primarily with precipitating downdrafts. In upper levels the dotted curves indicate slightly larger values than those for the corresponding M_u and M_d profiles. As in Fig. 6a, this effect is due to the presence of diffuse clouds at these levels.

The mass fluxes M_u, M_d and M_e were also calculated for two-dimensional convection (run B) and are shown in Fig. 9. The M_u profile has a single maximum near 1.5 km and then a very slow decrease with height up to 10 km. In both Figs. 8 and 9 the mass fluxes decrease rapidly with height above 10 km. The M_d curve has a minimum near 1.1 km and is nearly constant with height between 5 and 10 km. The relative amplitude of the M_e curve is smaller in Fig. 9 than in Fig. 8.

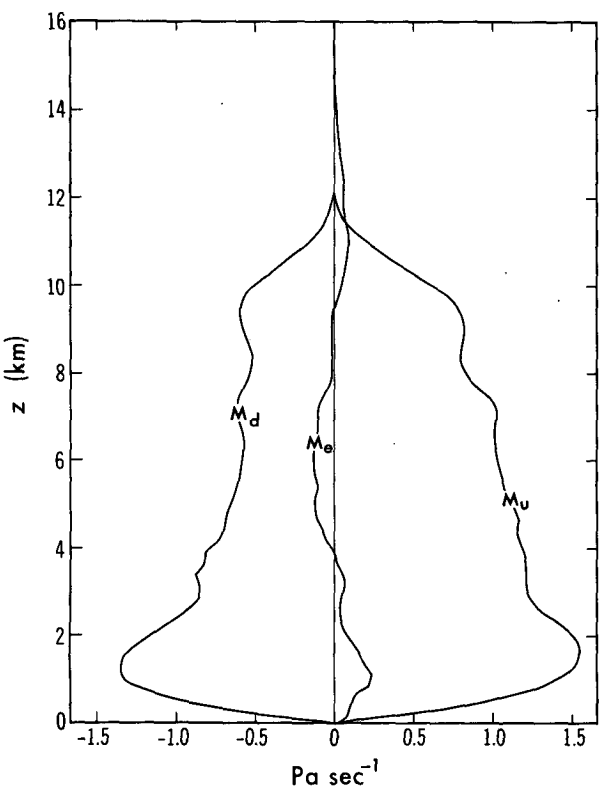

FIG. 9. The time-mean vertical mass flux for the last 80 min of run B. Curves for M_u, M_d and M_e are specified the same as in Fig. 8.

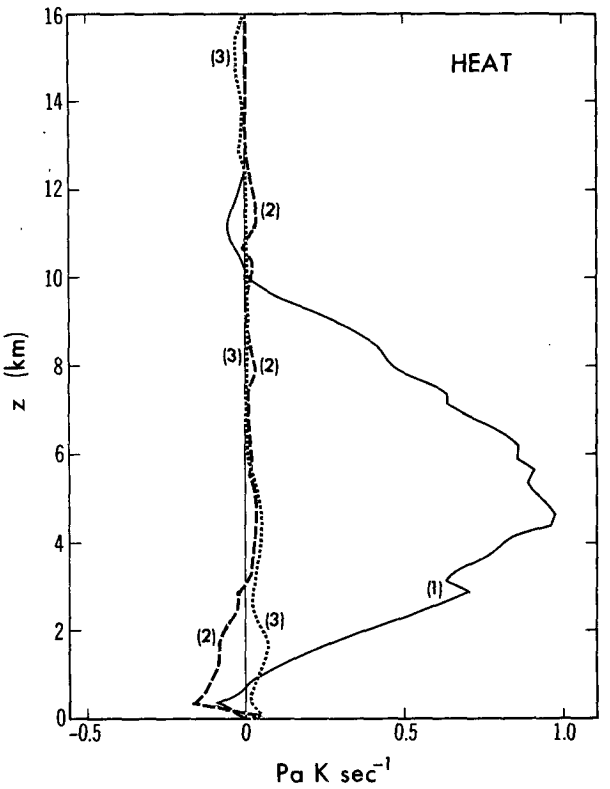

FIG. 10. The vertical heat flux in cloud plus rain ($q_c + q_r > 10^{-2}$ g kg^{-1}) updrafts, downdrafts and environment for run A: (1) in updrafts; (2) in downdrafts; (3) in environment. Time averages obtained from data at 8 min intervals.

Finally, comparing these two figures, it is seen that the values of M_u and M_d are about 40% larger in magnitude for two-dimensional than for three-dimensional convection.

The corresponding vertical heat and moisture flux profiles for run A are shown in Figs. 10 and 11. In distinction to the corresponding data of Soong and Tao (1980), the present profiles include grid-scale fluxes only. The subgrid-scale fluxes of heat and moisture will be discussed briefly below. For the present figures the vertical fluxes associated with in-cloud plus rain updrafts are dominant, with a maximum heat flux of 0.97 Pa K s^{-1} at 4.5 km and a maximum moisture flux of 1.94 Pa g kg^{-1} s^{-1} at 3.4 km. Note that both of these maximum values occur in the vertical region of low cloud fraction CF shown in Fig. 6a, giving further evidence that this is a region of active convection.

The curves for the environmental vertical heat and moisture fluxes show small values of these fluxes. The in-cloud plus rain flux of moisture due to downdrafts has significant negative values above 2.2 km and positive values below 2.2 km. The negative values in middle levels can be expected due to moist air (detrained from clouds) sinking. In the lower levels the moisture flux is positive due to relatively dry air sinking below

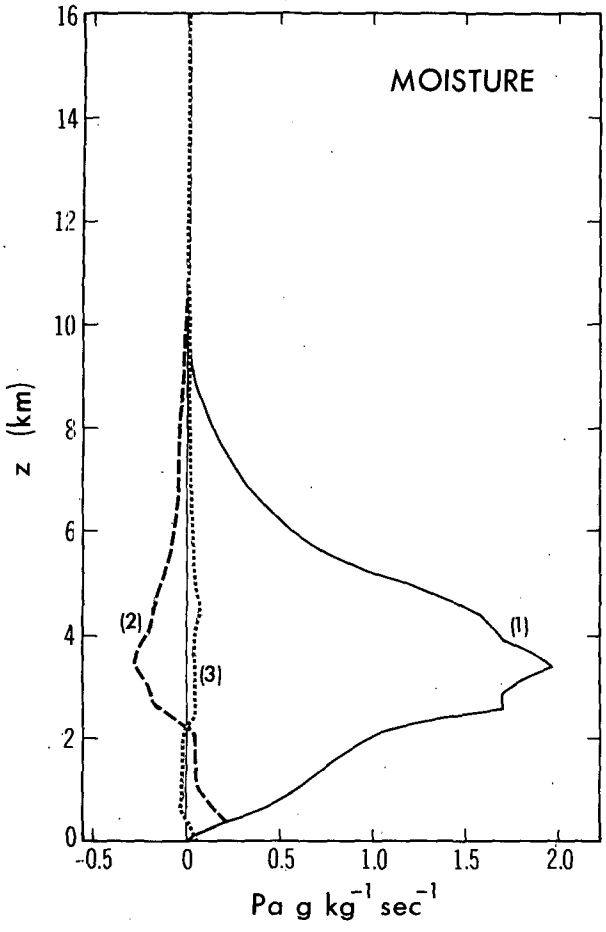

FIG. 11. As in Fig. 10 except for vertical moisture fluxes.

cloud base. The in-cloud plus rain heat flux due to downdrafts is slightly positive above 3 km, significantly negative between $z = 0.15$ km and $z = 3$ km and slightly positive just above the surface. The negative values of heat flux are due to relatively warm air sinking below cloud base. That this is the case is seen consistently in cross sections showing precipitating downdrafts. This effect was also found in the numerical calculations of Lipps and Hemler (1982) and discussed in that study. The cool air near the surface associated with downdrafts is very weak, indicating that this effect may be poorly represented in the present model results.

The total horizontal-average grid-scale fluxes of heat and moisture (solid lines) and the corresponding subgrid-scale fluxes (dashed lines) are shown in Figs. 12a and 12b. Note that the subgrid-scale heat and moisture fluxes have a significant contribution below 3.5 km with maximum values roughly one-quarter the magnitude of the corresponding maximum grid-scale fluxes. Soong and Tao (1980) state that their turbulent fluxes are, in general, one order of magnitude smaller than the grid-scale fluxes. Evidently the present model has stronger turbulent mixing associated with moist instability which causes the stronger subgrid-scale fluxes. In Fig. 12a the strong negative subgrid-scale heat flux at $z = 250$ m is a reaction to the strong evaporative cooling at $z = 125$ m as indicated by Figs. 6b and 7. Time-mean values of the surface heat and moisture fluxes are indicated by the nonzero values of the subgrid-scale fluxes at $z = 0$.

6. Discussion of vertical velocity cores

In the observational study of LeMone and Zipser (1980), vertical velocity cores are defined as the stronger portions of the updrafts and downdrafts with the magnitude of the vertical velocity continuously greater than 1 m s^{-1} over a distance of at least 0.5 km. So that the numerically simulated vertical velocities can be compared with their observational data, we also define vertical velocity cores in the same way. It should be noted, however, that since $\Delta x = \Delta y = 0.5$ km in the present study, there may be considerable truncation effects when considering the smaller scale cores. Again, the primary emphasis will be upon data taken from the last 80 min of run A as in section 5.

a. Some characteristics of vertical velocity cores

Time-mean data for vertical velocity cores were calculated for the entire horizontal domain over the last 80 minutes of runs A–C. In addition, for run A, data for in-cloud only ($q_c > 0$) upward vertical velocity cores were also calculated. Time-mean upward mass flux data for the last 80 minutes of run A are shown in Fig. 13. As in Fig. 8, the short-dashed curve represents the total in-cloud upward mass flux. The solid curve is the in-cloud upward mass flux associated with upward cores and the dashed curve represents upward mass flux associated with upward cores over the entire hor-

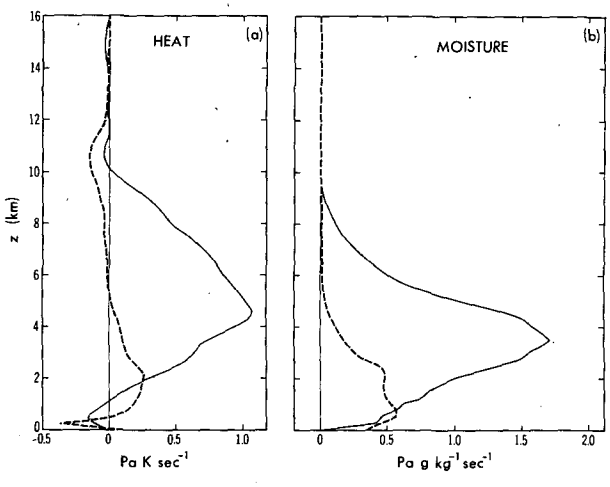

FIG. 12. The horizontal-average grid-scale vertical fluxes of heat and moisture (solid lines) and the corresponding subgrid-scale fluxes (dashed lines) for the last 80 min of run A. (a) Heat fluxes and (b) moisture fluxes.

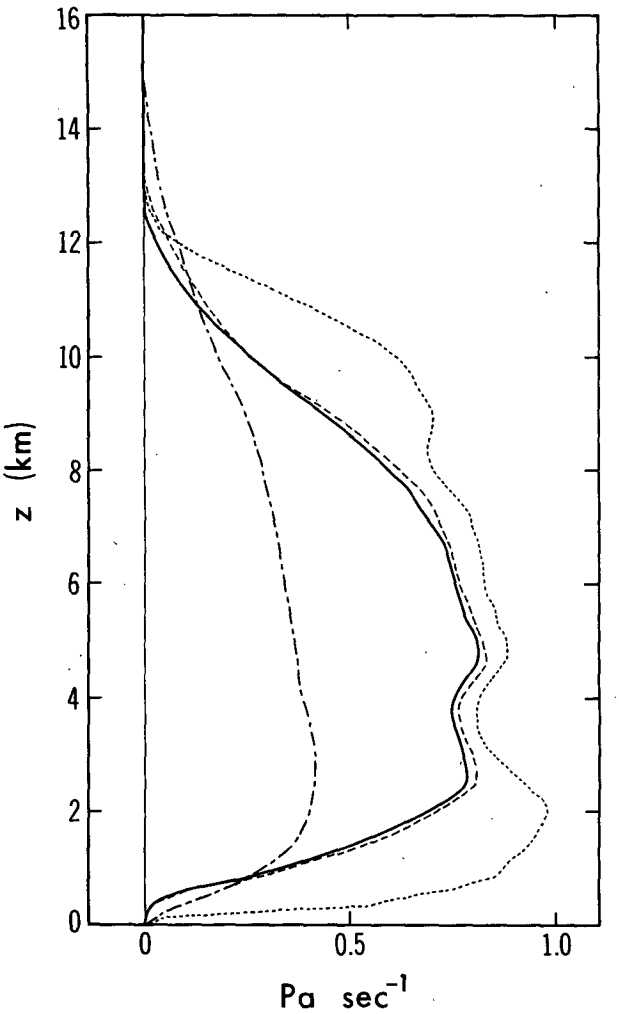

FIG. 13. Time-mean upward mass flux for last 80 min of run A: Short-dashed curve, total in-cloud ($q_c > 0$) upward mass flux; solid curve, in-cloud mass flux associated with upward vertical velocity cores; dashed curve, mass flux due to upward cores over the entire horizontal domain; dash-dot curve, mass flux associated with W. Time averages obtained from data at 8 min intervals.

izontal domain. Also shown by the dash-dot curve is the net mass flux associated with the mean vertical velocity W.

This figure shows clearly that for run A the upward vertical velocity cores are virtually all in-cloud. The vertical mass flux for upward cores over the entire horizontal area is approximately 2% larger at most levels than the corresponding in-cloud mass flux due to upward cores. That these two curves are nearly coincident may be due to the lack of vertical wind shear in the present simulation. A comparison of the solid and short-dashed curves indicates that between 2.5 km and 8 km the in-cloud upward mass flux is nearly all associated with the upward velocity cores. At lower and higher levels, however, the mass flux associated with weaker vertical velocities dominates. For the upper levels this result is not unexpected since the flow becomes more stratiform with height. For the lower levels the weak nature of the upward cores appears to be at odds with the observations of LeMone and Zipser (1980). This characteristic of the present simulation will be discussed in more detail in section 6b.

Another interesting result seen in Fig. 13 is that for the region 2.5 km $\leqslant z \leqslant$ 8.0 km, where the in-cloud upward mass flux is nearly all associated with upward cores, the upward mass flux associated with cores is approximately double the net mass flux associated with W. A similar result was found by Zipser et al. (1981) for their mass flux data at 1 and 3 km during the early stages of their observed moist convective rainband. This ratio is a significant quantity since, as these authors point out, it is the mass flux associated with W (the net mass flux) which can be determined in a larger scale model.

In Fig. 14 are shown the time-mean fractional areas of upward and downward cores over the last 80 minutes of runs A–C. An immediate result seen from this figure is that the fractional areas of vertical velocity cores in run A are much smaller than for the corresponding two-dimensional calculations. In addition, the fractional areas are larger at the higher elevations in run C than in run B, which is compatible with the stronger convection in run C (see Fig. 3 and Table 1). In run A the fractional area of updraft cores is nearly constant with height, varying between 2.5% and 4.0% from z = 1 km to z = 11 km. The fractional areas of downdraft cores in run A are approximately two-thirds that of the updraft cores.

b. Comparison with observations

The present data for vertical velocity cores are now compared with the observational data of LeMone and Zipser (1980) and Zipser and LeMone (1980). In their studies various quantities have been evaluated at the median (50% of cores stronger than value) and at the 10% level (10% of cores stronger than value) for the distribution of cores observed within a given height interval. The height intervals so analyzed are 300 $\leqslant z \leqslant$ 700 m, 700 $< z \leqslant$ 2500 m, 2500 $< z \leqslant$ 4300 m and 4300 m $< z \leqslant$ 8100 m.

In this study we compare computed and observed values for the mean vertical velocity $\bar{w}$ and the mean diameter $\bar{D}$ for both upward and downward cores. The numerical data for $\bar{w}$ and $\bar{D}$ at the median and 10% levels are calculated for the entire horizontal domain at z = 0.5, 1.5, 4.0, 6.5 and 9.0 km. In these calculations the cores are ordered in the distribution according to the magnitude of either $\bar{w}$ or $\bar{D}$. Since the cores are discrete entities, the definitions chosen for the median and 10% levels are given by

$$\text{Median} = 0.5N + 0.5 \tag{6.1}$$

$$10\%\ \text{Level} = 0.9N + 0.5 \tag{6.2}$$

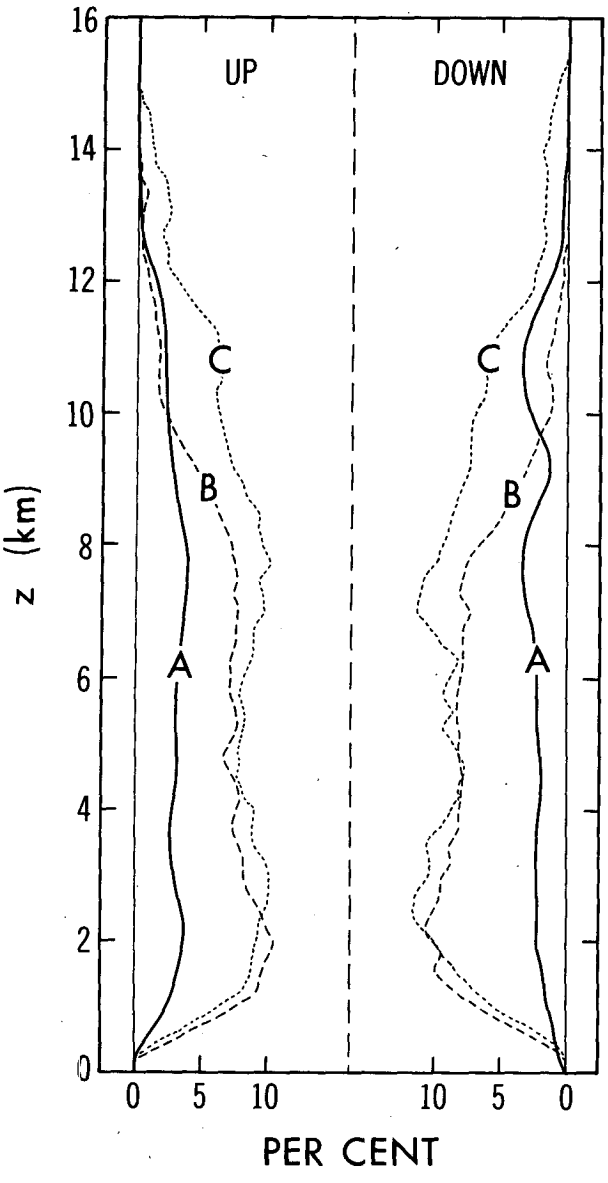

FIG. 14. Time-mean fractional areas of updraft cores (left) and downdraft cores (right) for the last 80 min of runs A–C. Time averages obtained from data at 8 min intervals for runs A and C.

where N is the total number of cores in the distribution. Since in general the expressions (6.1) and (6.2) will give noninteger values, the corresponding values of $\bar{w}$ and $\bar{D}$ are obtained by linear extrapolation using data associated with the appropriate cores in the distribution.

In Table 3 are shown the total number of upward and downward cores analyzed in run A. For all cases, data for the cores were obtained at eight minute intervals. As in section 5, the data at 160 and 240 minutes were given a weight of one-half since these times are at the end points of the 80 minute averaging interval. Thus half-integer values are seen in this table.

Data for the core diameter $\bar{D}$ and the mean vertical velocity $\bar{w}$ for run A are plotted in Figs. 15a and 15b, respectively. The corresponding observational data from LeMone and Zipser (1980) are shown in Figs. 15c and 15d. Data for the median and the 10% level are indicated by circles and triangles in this figure. The data of Gray (1965) for convection observed in hurricanes are shown by the filled symbols at $z = 4.5$ km in Fig. 15d. It is seen that his data are somewhat larger but in general agreement with the observed data of LeMone and Zipser (1980). As discussed by Zipser and LeMone (1980), however, the data from the Thunderstorm Project (Byers and Braham, 1949) have values of $\bar{w}$ which are nearly a factor of 3 larger than observed for GATE convection. Thus the vertical velocities for tropical maritime convection are evidently much weaker than for continental deep convection.

In comparing numerical and observational data in Fig. 15, it must be noted that these two types of data were obtained by different methods. The observational data were obtained from linear flight paths through cloudy areas and then these data were analyzed for $\bar{D}$ and $\bar{w}$. The numerical data, on the other hand, were obtained by horizontal averages on specific z-levels. Thus, the definition of $\bar{D}$ for a given core is

$$\bar{D} = n^{1/2}\Delta \tag{6.3}$$

where n is the number of grid points contained by the core on the z-level. The grid interval $\Delta = \Delta x = \Delta y = 500$ m. Hence, for the numerical data, $\bar{D}$ is simply the square root of the area of the given core.

In comparing Fig. 15a with Fig. 15c we see that the numerical values of $\bar{D}$ in run A are in relatively good agreement with the observations. For updraft cores, values of $\bar{D}$ vary between approximately 1 km (median) to about 2 km (10% level). Values of $\bar{D}$ are somewhat smaller for downdraft cores. Also, as shown in this figure, median values of $\bar{D}$ are nearly independent of height for both run A and the observations. At the 10% level, the numerical values of $\bar{D}$ are somewhat larger than observed at upper levels and smaller than observed at lower levels for both updraft and downdraft cores.

When comparing Fig. 15b with Fig. 15d for values of $\bar{w}$, however, it is seen that the agreement of numerical data with observations is not nearly as good as for values of $\bar{D}$. For downward velocity cores, the numerical values of $\bar{w}$ are much smaller than the observed, being nearly a factor of 2 smaller than the observations at

TABLE 3. Numbers of cores in run A.

z (km)	Updrafts	Downdrafts
0.5	30.5	40.0
1.5	78.5	75.0
4.0	69.0	71.5
6.5	54.5	63.0
9.0	42.0	34.5

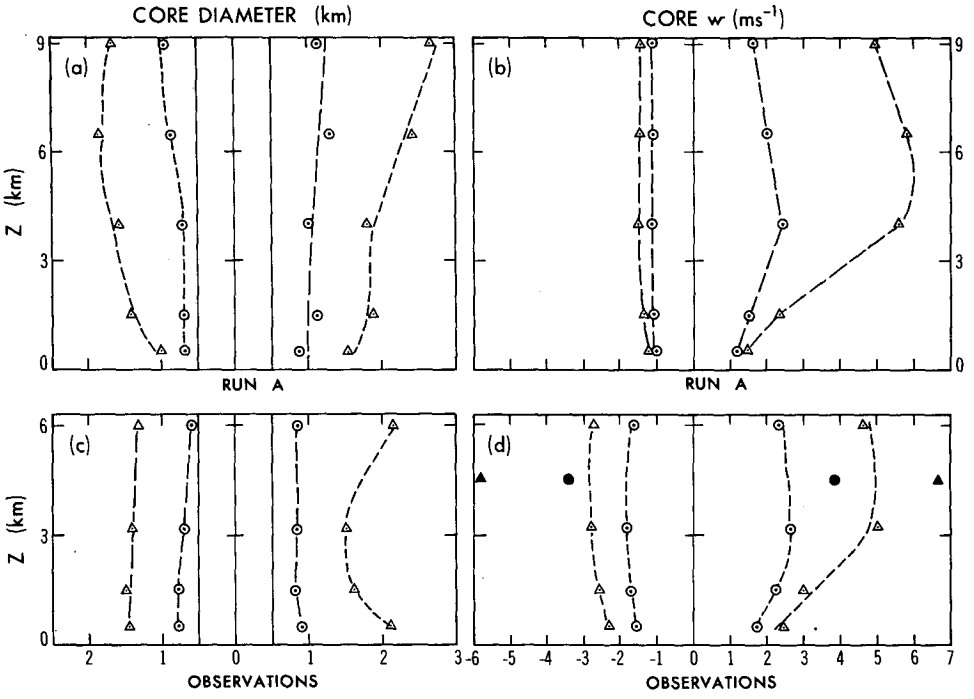

FIG. 15. Variation with height of median (50%) and 10% level (10% of cores stronger than value) for updraft and downdraft cores in run A: (a) core diameter $\bar{D}$ and (b) mean vertical velocity $\bar{w}$. Corresponding values in (c) and (d) are given for the observed data of LeMone and Zipser (1980). Solid symbols represent data of Gray (1965) at the 4.5 km level.

the 10% level. The vertical variation of $\bar{w}$, however, does appear to follow the observations for downdraft cores. When considering updraft cores, the values of $\bar{w}$ in run A at $z = 0.5$ km and at $z = 1.5$ km are too small compared with the observations, whereas values at the upper levels are in reasonable agreement.

Values of $\bar{w}$ for updraft and downdraft cores at the median and 10% levels were also obtained for the two-dimensional calculations, run B and run C. For these simulations, the values of $\bar{w}$ were too small compared with the observations at $z = 0.5$ km and $z = 1.5$ km, as was the case for run A. In general, the two-dimensional updraft cores are somewhat weaker and the downdraft cores somewhat stronger than the corresponding values shown in Fig. 15 for run A. Specifically, downdraft cores at the 10% level for z = 4.0 km and above are approximately 50% stronger than their counterparts in run A. As discussed in section 4c, these stronger downdrafts may explain the larger cloud evaporation CE and lower cloud efficiency E found in two- versus three-dimensional convection.

A positive feature of the present simulation is that the updraft values of $\bar{w}$ are in good agreement with observations at the upper levels. This is particularly relevant as the observed GATE convection has small values of $\bar{w}$ compared with deep continental convection, as discussed above. According to LeMone and Zipser (1980) only one core with $\bar{w}$ of 9 m s^{-1} and two cores with w_{max} of 17 m s^{-1} were found in all of GATE. These values are consistent with the results of run A. The maximum value of the vertical velocity, w_{max}, is 19.6 m s^{-1} as shown in Table 1. Also, values of $\bar{w}$ slightly greater than 9 m s^{-1} occurred for only three cores: one each at the 4.0 km, 6.5 km and 9.0 km levels.

In all three simulations the updraft values of $\bar{w}$ at the lower levels are much smaller than found by LeMone and Zipser (1980). The observed upward values of $\bar{w}$ near 2 m s^{-1} at $z = 0.5$ km must be associated with mechanical lifting as the convective instability is not capable of generating such large values of $\bar{w}$ near cloud base. For observed rainbands such forced lifting is associated with outflow gust fronts. Weisman and Klemp (1982) show that relatively weak low-level wind shear is ideally suited for the redevelopment of convective cells along the leading edge of outflow gust fronts. The data in Fig. 1 of Soong and Tao (1984) indicate that such low-level wind shear does exist in the subcloud layer for the u-velocity. Thus in the present simulations the absence of outflow gust fronts with the observed vertical lifting may be associated with the neglect of this subcloud layer wind shear in the model initial data.

7. Summary

A set of four-hour numerical simulations has been carried out for a tropical maritime atmosphere (Fig. 1)

with a large-scale vertical velocity W present (Fig. 2). The base state has no vertical wind shear. Detailed comparisons are made between the three-dimensional calculation, run A, and the two-dimensional calculations, run B and run C. In each case the convection is initiated by a random moisture disturbance. As shown in Fig. 3, two-dimensional convection takes 100 minutes and three-dimensional convection takes 135 minutes to develop. This long start-up time for deep convection is considered to be a realistic feature of the simulations, being associated with a vertical lifting of 200 m in the lowest few kilometers due to the large-scale W. Zipser et al. (1981) suggested that this amount of vertical lifting was necessary before deep convection could develop in their observed rainband.

For run A, definable patterns were obtained when a vertical space average and a time mean over the last two hours were taken. The cells shown in Fig. 4 are relatively isolated and randomly distributed. With vertical wind shear included, it is likely that the cells would form more of a line structure (Tao, 1983). The average cell diameter is roughly 2.5 km, which appears to represent the strong updrafts at upper levels (see Fig. 15a). At the surface an average shower lasted about 40 minutes and gave approximately 4.0 cm of rainfall near its center. In Fig. 5 the cloud efficiency for run A is seen to be 42% over the entire four-hour simulation, with cloud water evaporation CE and rain water evaporation RE accounting for over 50% of the cloud condensation CC.

In section 5 time-mean statistics for deep moist convection were calculated for the last 80 minutes of runs A and B with the primary emphasis placed upon run A. When examining the mean cloud properties, it was found that the mean cloud fraction CF was less than 10% between $z = 2.4$ km and $z = 6.4$ km for run A. In spite of these low values of cloudiness, this vertical layer is a region of very active convection. This conclusion is shown very clearly by the in-cloud plus rain vertical fluxes of heat and moisture plotted in Figs. 10 and 11: maximum heat and moisture fluxes associated with updrafts occur at $z = 4.5$ km and at $z = 3.4$ km, respectively.

The vertical variation of the time-mean temperature and moisture budgets for run A is plotted in Fig. 7. For the temperature budget the primary features are a strong net heating between 4 and 8 km and a strong net cooling near the surface. These features indicate that the atmosphere is being stabilized and are directly associated with the strong positive net condensation $\langle \mathrm{NC} \rangle$ in middle levels and strongly negative $\langle \mathrm{NC} \rangle$ due to evaporation near the surface. For the moisture budget a prominent feature is the net drying near the surface where downward flux of dry air dominates the evaporation. Net drying also occurs above 5.5 km. Between 2 and 5.5 km moistening due to $\rho_0 S_m$ dominates the drying associated with the sum of $\langle \mathrm{NC} \rangle$ and vertical advection of moisture.

The present temperature and moisture budgets can be compared with the data of Soong and Tao (1980) as shown in their Fig. 10. It is seen that for their data the net warming between 4 and 8 km is much less and a strong net moistening occurs between 2 and 4 km. These features are consistent with their budgets being calculated over the entire six-hour run. Here the data have been averaged over the last 80 minutes of run A which is a period of active convection.

The time-mean vertical mass flux profiles inside the cloud plus rain area are shown in Fig. 8 for run A. Near cloud base the curve for upward mass flux M_u is in approximate balance with the curve for downward mass flux M_d. Above cloud base the values of M_u are approximately double those of M_d until the region of high-level outflow is reached ($z \geq 10$ km) where M_u and M_d are roughly equal. The profile for the environmental mass flux M_e shows a significant downward mass flux for the middle layers (4–9 km). Near the surface M_e is positive due to forced vertical lifting outside the region of the precipitating downdrafts. The present curves for M_u, M_d and M_e can be compared with the data of Soong and Tao (1980) shown in their Fig. 12. Noteworthy differences are the relatively larger amplitude of the M_e curve and the double maxima of the M_u curve in the present study.

Vertical profiles of in-cloud upward and downward mass fluxes are also shown in Fig. 8. Most of the upward mass flux occurs inside of clouds. From $z = 0.5$ km to $z = 6.5$ km, the excess of the M_u mass flux over the in-cloud upward mass flux is approximately 12% of the total M_u mass flux. At upper levels the M_u and M_d curves are nearly the same as the corresponding in-cloud mass flux profiles. At lower levels the minimum in the M_d curve is much stronger than the corresponding minimum in the in-cloud downward mass flux. Thus M_d is primarily associated with precipitating downdrafts at low levels.

In section 6 vertical velocity cores from the numerical simulations are analyzed and compared with observations. Time-mean upward mass flux data for run A are shown in Fig. 13. Comparing the mass flux curves for in-cloud updraft cores and for updraft cores over the entire horizontal domain, it is seen that virtually all updraft cores are in-cloud. An examination of Fig. 13 also indicates that between $z = 2.5$ km and $z = 8.0$ km the total in-cloud vertical mass flux is nearly all associated with vertical velocity cores. In this same vertical region, the upward mass flux associated with cores is approximately double the net mass flux associated with W. A similar result was found by Zipser et al. (1981).

The time-mean fractional areas of updraft and downdraft cores for the last 80 minutes of runs A–C are shown in Fig. 14. The fractional areas of vertical velocity cores in run A are much smaller than for the corresponding two-dimensional calculations. For run A the fractional area of updraft cores is nearly constant

with height, varying between 2.5% and 4.0% from z = 1 km up to z = 11 km. Other features of the data in this figure are discussed in section 6.

Data for the diameter $\bar{D}$ and mean vertical velocity $\bar{w}$ for vertical velocity cores during the last 80 minutes of run A are given in Figs. 15a and 15b. The corresponding observational data from LeMone and Zipser (1980) are shown in Figs. 15c and 15d. The numerical values of $\bar{D}$ in run A are in relatively good agreement with the observations. When comparing numerical against observed values of $\bar{w}$, however, the agreement is not nearly as good. For downdrafts cores, the values of $\bar{w}$ are nearly a factor of two smaller than the observed at the 10% level. For updraft cores, the values of $\bar{w}$ for run A at z = 0.5 km and at z = 1.5 km are too small compared with the data of LeMone and Zipser (1980) whereas values in the upper levels are in reasonable agreement.

For future work there are three significant areas in which the present study can be expanded. These are 1) the inclusion of vertical wind shear, 2) the use of open lateral boundary conditions, and 3) the inclusion of the ice phase in the bulk cloud physics. As shown in Fig. 1 of Soong and Tao (1984), significant vertical shear exists for both horizontal velocity components. In section 6 it was suggested that the neglect of the subcloud layer u-velocity wind shear in the present calculations may be the reason for the weak vertical lifting the small values of upward $\bar{w}$ associated with the simulated gust fronts. The present numerical model has been modified to include open lateral boundary conditions. With these boundary conditions and the observed wind shear, it may be possible to develop stronger gust fronts at the surface and thus obtain more realistic values for $\bar{w}$ in updraft cores. Finally, as discussed by Zipser and LeMone (1980), the small observed values of $\bar{w}$ in cores suggest that the ice phase is important in tropical convection above the freezing level. Hence inclusion of the ice phase may also lead to a more complete understanding of the dynamics of tropical maritime convection.

Acknowledgments. Our thanks go to I. Held, Y. Kurihara and G. Lau of the Geophysical Fluid Dynamics Laboratory for reading the manuscript and making many helpful suggestions. The primary calculations were carried out on a TI/ASC computer. The figures were drafted by Philip G. Tunison and staff and the manuscript typed by Joan Pege.

APPENDIX

Discussion of Subgrid-Scale Mixing and Bulk Cloud Physics

1. Subgrid-scale mixing processes

The present subgrid-scale turbulence parameterization is modified from that of Lipps and Hemler (1982) in regions of subsaturated flow with stable static stability. In these regions it is assumed that the mixing processes are much weaker in the vertical than in the horizontal. This assumption has the advantage of largely eliminating the excessive vertical mixing of the base state temperature, water vapor and momentum fields which can occur in numerical models. From a physical point of view, this procedure is realistic in that it is expected that stable static stability will inhibit vertical mixing.

Inside the clouds and in unstably stratified subsaturated regions the turbulence is isotropic with strong mixing in both the vertical and horizontal. Where the vertical mixing is weak, the turbulence is transversely isotropic (Kirwan, 1969; Williams, 1972). For this case the subgrid-scale Reynolds' stress τ_{ij} has the components

$$\left.\begin{aligned}
\tau_{11} &= \rho_0 K\left(2\frac{\partial u}{\partial x} - \frac{2}{3}\mathrm{DIV}\right)\\
\tau_{22} &= \rho_0 K\left(2\frac{\partial v}{\partial y} - \frac{2}{3}\mathrm{DIV}\right)\\
\tau_{33} &= \rho_0 K\left(2\frac{\partial w}{\partial z} - \frac{2}{3}\mathrm{DIV}\right)\\
\tau_{12} &= \tau_{21} = \rho_0 K\left(\frac{\partial v}{\partial x} + \frac{\partial u}{\partial y}\right)\\
\tau_{13} &= \tau_{31} = \rho_0 K_v\left(\frac{\partial w}{\partial x} + \frac{\partial u}{\partial z}\right)\\
\tau_{23} &= \tau_{32} = \rho K_v\left(\frac{\partial w}{\partial y} + \frac{\partial v}{\partial z}\right)
\end{aligned}\right\} \qquad \text{(A1)}$$

where

$$\mathrm{div}\left(= \frac{\partial u}{\partial x} + \frac{\partial v}{\partial y} + \frac{\partial w}{\partial z}\right)$$

is the divergence, and K and K_v are the horizontal and vertical coefficients of eddy viscosity. The third coefficient of eddy viscosity ϵ discussed by Kirwan and Williams has been set equal to zero in (A1). According to Williams (1972), $\epsilon \approx 0$ can be expected for a stable atmosphere. Also from Eq. (21) in his paper it can be seen that the viscous dissipation Φ is the largest for ϵ = 0. When the turbulence is isotropic, Eq. (A1) remains the valid expression for τ_{ij} but in this case $K_v = K$.

As noted in section 2c a staggered finite-difference grid system is used so that grid points for w and ϕ alternate in the vertical. The variables θ_l, q_v, q_c, q_r are evaluated at ϕ-grid points whereas K and K_v are evaluated at w-grid points. The most general form of K includes both deformation and unstable stratification effects (Lilly, 1962; Clark, 1979). Thus K is specified as in Lipps and Hemler (1982) and is given by Eq. A(22) of that study. The vertical coefficient of eddy viscosity K_v is specified by

$K_v = FK$

$$F = \left\{1 + 10\delta_1 \frac{g\partial\theta_v/\partial z}{[10^{-6} + (\partial u/\partial z)^2 + (\partial v/\partial z)^2]}\right\}^{-1} \quad \text{(A2)}$$

where $\delta_1 = 0$ if cloud water q_c is present either directly above or below the K_v grid point, or if static instability in clear air is present. Static instability is indicated by a negative vertical gradient of virtual potential temperature θ_v. This condition is given by

$$\frac{\partial\theta_v}{\partial z} = \frac{\partial}{\partial z}(\theta_0 + \theta_1) + 0.608\theta_0 \frac{\partial q_v}{\partial z} < 0. \quad \text{(A3)}$$

Thus in cloudy regions and in unstable clear air the turbulence is isotropic with $K_v = K$. In statically stable clear air the turbulence is transversely isotropic with $\delta_1 = 1$ and $K_v \ll K$. In this case typical values are $K_v \sim 10^{-3}$ K.

In Eqs. (2.10)–(2.13) the turbulent diffusion is represented through gradients of the subgrid-scale correlations $-\rho_0\overline{u_j'\theta'}$, $-\rho_0\overline{u_j'q_v'}$, $-\rho_0\overline{u_j'q_c'}$ and $-\rho_0\overline{u_j'q_r'}$. These correlations are specified by Eqs. (A14)–(A17) of Lipps and Hemler (1982). In their equations the coefficient of eddy diffusivity K_h is given by $3K$ for the horizontal components ($j = 1, 2$) of the above correlations. The factor of 3 represents the ratio of eddy diffusivity to eddy viscosity as used by Deardorff (1972).

In accordance with the present discussion of the subgrid-scale mixing, the expressions given in Lipps and Hemler (1982) for $-\rho_0\overline{w'\theta'}$ and $-\rho_0\overline{w'q_v'}$ have K_h given by $3K_v$. For $-\rho_0\overline{w'q_c'}$ and $-\rho_0\overline{w'q_r'}$ we set

$$-\rho_0\overline{w'q_c'} = 3\rho_0 K\frac{\partial q_c}{\partial z} \quad \text{(A4)}$$

$$-\rho_0\overline{w'q_r'} = 3\rho_0 K\frac{\partial q_r}{\partial z}. \quad \text{(A5)}$$

Note that K_v has been set equal to K in (A4), as nonzero values of $-\rho_0\overline{w'q_c'}$ can only occur if cloud water q_c is present. Although rain water q_r often occurs out of cloud, we have assumed that vertical mixing of q_r is strong so that $K_v = K$ for all points in Eq. (A5).

2. The bulk cloud physics

The warm rain bulk cloud physics is a modified form of the parameterization given by Kessler (1969) in which the liquid water is separated into cloud water q_c and rain water q_r. Since MKS units are used in the present discussion, q_c and q_r have units of kg/kg. Expressions for S_a, S_c, V_T and E are obtained from the theory of Manton and Cotton (1977; hereafter referred to as MC). A summary of their development can be found in Tripoli and Cotton (1980). As will be discussed below, MC indicated that the expressions for S_c, V_T and E lose their validity for $\rho_0 q_r$ less than about 10^{-3} kg m^{-3}. In the present model these expressions will be modified so as to have reasonable validity for all values of q_r.

The autoconversion S_a gives rise to the initial formation of rain water q_r by the coalescence between cloud droplets to form raindrops. This process is given by the expression

$$S_a = 7.00\rho_0^{4/3} q_c^{7/3} h(q_c - q_{cm}) \quad \text{(A6)}$$

where $h(x)$ is the Heaviside unit step function and q_{cm} is the minimum value of q_c below which there is no autoconversion. In (A6) and in the expressions for V_T, S_c, E to follow, constant parameters have been assigned the values given by MC.

From the discussion in MC it is seen that $\rho_0 q_{cm}$ is proportional to the mean droplet concentration N_c. Following MC we take $N_c = 10^8$ m^{-3} and $\rho_0 q_{cm} = 0.42 \times 10^{-3}$ kg m^{-3}.

For the calculation of S_c, V_T and E it is assumed that the raindrop spectral density $\phi(r)$ has an exponential distribution (Marshall and Palmer, 1948):

$$\phi(r) = (N_R/R_m)\exp(-r/R_m) \quad \text{(A7)}$$

where N_R represents the raindrop concentration and R_m is a characteristic radius for the distribution. In contrast to Kessler, MC assumed that the slope of the distribution ($1/R_m$) is a constant whereas the intercept parameter

$$N_0 = N_R/R_m \quad \text{(A8)}$$

is a variable. This assumption is supported by the experimental data of Blanchard and Spencer (1970), which suggest that the Marshall–Palmer distribution is an asymptotic spectral density produced by a balance between coalescence and drop breakup. In addition, the numerical results of Srivastava (1978) indicate that the slope of (A7) tends toward a constant when collisional breakup becomes dominant. This occurs when $\rho_0 q_r > 10^{-3}$ kg m^{-3}. By an independent argument MC also find that the lower limit to the validity of the present parameterization occurs for $\rho_0 q_r \approx 10^{-3}$ kg m^{-3}.

Srivastava (1978) noted that the data of Blanchard and Spencer (1970, Fig. 9) suggest a constant slope ($1/R_m$) $\approx 3.8 \times 10^{-3}$ m^{-1}. This value is used in the present study so that $R_m = 2.63 \times 10^{-4}$ m. This is virtually identical to the value used by MC and Tripoli and Cotton (1980).

Using the data of Gunn and Kinzer (1949) for the terminal velocity of raindrops and the cloud physics approach of MC, we obtain for the fall velocity V_T of the rain water q_r

$$V_T = 6.185\left(\frac{\rho_0}{\rho_{00}}\right)^{-1/2} \quad \text{(A9)}$$

where $\rho_{00} = 1.15$ kg m^{-3}. In this expression for V_T and in those to follow for S_c and E the base state density variation with height is retained. This effect has been neglected in MC and Tripoli and Cotton (1980).

Following Kessler (1969), MC obtained S_c by integrating the rate of increase in mass of a single drop of radius r due to accretion over the entire distribution (A7):

$$S_c = 5.786\left(\frac{\rho_0}{\rho_{00}}\right)^{1/2} q_c q_r. \quad \text{(A10)}$$

The evaporation of rain has been treated as in MC where the effective diffusivity D_{e0} has been set equal to 0.113×10^{-4} m^2 s^{-1}. Tripoli and Cotton carry out a more rigorous calculation in which D_{e0} is treated as a variable to obtain the evaporation of rain. In the present study

$$E = 0.3362\left(\frac{\rho_0}{\rho_{00}}\right)^{5/4}(q_{vs} - q_v)q_r \qquad \text{(A11)}$$

which corresponds to Eq. (3.31) in MC.

The previous discussion indicates that (A9)–(A11) are valid only when $\rho_0 q_r > 10^{-3}$ kg m^{-3}. In addition to the theoretical considerations, Eqs. (A9) and (A11) have some apparent defects when q_r is very small. As seen in (A9), the fall velocity V_T is independent of q_r since R_m is constant. It would seem more appropriate that $V_T \to 0$ as $q_r \to 0$. The difficulty with (A11) is that E is proportional to q_r so that the evaporation is very weak with small q_r. Note that in Kessler's formulation E is proportional to $q_r^{0.65}$.

In order to offset these theoretical and practical difficulties with (A9)–(A11) we have decided upon an admittedly ad hoc correction. It seems physically reasonable that $R_m \to 0$ as $q_r \to 0$. We make the assumption

$$R_m = R_0[\tanh(\beta q_r)]^{1/2} \qquad \text{(A12)}$$

where $R_0 = 2.63 \times 10^{-4}$ m and $\beta = 10^{-3}$. Including (A12) in the derivation of (A9)–(A11) gives the relations

$$V_T = 6.185(\rho_0/\rho_{00})^{-1/2}[\tanh(\beta q_r)]^{1/4} \qquad \text{(A13)}$$

$$S_c = 5.786(\rho_0/\rho_{00})^{1/2}[\tanh(\beta q_r)]^{-1/4}q_c q_r \qquad \text{(A14)}$$

$$E = 0.3362(\rho_0/\rho_{00})^{5/4}[\tanh(\beta q_r)]^{-5/8}(q_{vs} - q_v)q_r. \qquad \text{(A15)}$$

In the limit $q_r \to 0$ these expressions become

$$V_T \to 6.185(\rho_0/\rho_{00})^{-1/2}(\beta q_r)^{1/4} \qquad \text{(A13a)}$$

$$S_c \to 5.786(\rho_0/\rho_{00})^{1/2}\beta^{-1/4}q_c q_r^{3/4} \qquad \text{(A14a)}$$

$$E \to 0.3362(\rho_0/\rho_{00})^{5/4}\beta^{-5/8}(q_{vs} - q_v)q_r^{3/8}. \qquad \text{(A15a)}$$

These values of V_T, S_c and E appear to be appropriate for small q_r. Note that $V_T \to 0$ as $q_r \to 0$ and that (A15a) gives values of E larger than in Kessler's formulation for small q_r.

Thus, in summary, the basic equations of the present warm rain bulk cloud physics are Eqs. (A6) and (A13)–(A15) for S_a, V_T, S_c and E, respectively. The autoconversion S_a will not occur unless $\rho_0 q_c \geq 0.42 \times 10^{-3}$ kg m^{-3}.

REFERENCES

Blanchard, D. C., and A. T. Spencer, 1970: Experiments on the generation of raindrop size distribution by breakup. *J. Atmos. Sci.*, **27**, 101–108.

Byers, H. R., and R. R. Braham, 1949: *The Thunderstorm.* Government Printing Office, Washington, DC, 287 pp.

Chen, C.-H., and H. D. Orville, 1980: Effects of mesoscale convergence on cloud convection. *J. Appl. Meteor.*, **19**, 256–274.

Chen, Y.-L., and Y. Ogura, 1982: Modulation of convective activity by large-scale flow patterns observed in GATE. *J. Atmos. Sci.*, **39**, 1260–1279.

Clark, T. L., 1979: Numerical simulations with a three-dimensional cloud model: Lateral boundary condition experiments and multicellular severe storm simulations. *J. Atmos. Sci.*, **36**, 2191–2215.

Cho, H.-R., and Y. Ogura, 1974: A relationship between cloud activity and the low-level convergence as observed in Reed-Recker's composite easterly waves. *J. Atmos. Sci.*, **31**, 2058–2065.

Crowley, W. P., 1968: Numerical advection experiments. *Mon. Wea. Rev.*, **96**, 1–11.

Deardorff, J. W., 1972: Numerical investigation of neutral and unstable planetary boundary layers. *J. Atmos. Sci.*, **29**, 91–115.

Frank, W. M., 1978: The life-cycle of GATE convective systems. *J. Atmos. Sci.*, **35**, 1256–1264.

Gray, W. M., 1965: Calculation of cumulus vertical draft velocities in hurricanes from aircraft observations. *J. Appl. Meteor.*, **4**, 47–53.

Gunn, R., and G. D. Kinzer, 1949: The terminal velocity of fall for waterdrops in stagnant air. *J. Meteor.* **6**, 243–248.

Harlow, F. H., and J. E. Welch, 1965: Numerical calculation of time-dependent viscous incompressible flow of fluid with free surface. *Phys. Fluids*, **8**, 2182–2189.

Johnson, R. H., 1978: Cumulus transports in a tropical wave composite for Phase III of GATE. *J. Atmos. Sci.*, **35**, 484–494.

Kessler, E., 1969: *On the Distribution and Continuity of Water Substance in Atmospheric Circulations. Meteor. Monogr.*, No. 32, Amer. Meteor. Soc., 84 pp.

Kirwan, A. D., 1969: Formulation of constitutive equations for large-scale turbulent mixing. *J. Geophys. Res.*, **74**, 6953–6959.

Klemp, J. B., and R. B. Wilhelmson, 1978: The simulation of three-dimensional convective storm dynamics. *J. Atmos. Sci.*, **35**, 1070–1096.

LeMone, M. A., and E. J. Zipser, 1980: Cumulonimbus vertical velocity events in GATE. Part I: Diameter, intensity and mass flux. *J. Atmos. Sci.*, **37**, 2444–2457.

Lilly, D. K., 1962: On the numerical simulation of buoyant convection. *Tellus*, **14**, 148–172.

Lipps, F. B., 1977: A study of turbulence parameterization in a cloud model. *J. Atmos. Sci.*, **34**, 1751–1772.

——, and R. S. Hemler, 1980: Another look at the thermodynamic equation for deep convection. *Mon. Wea. Rev.*, **108**, 78–84.

——, and ——, 1982: A scale analysis of deep moist convection and some related numerical calculations. *J. Atmos. Sci.*, **39**, 2192–2210.

Mahlman, J. D., and R. W. Sinclair, 1977: Tests of various numerical algorithms applied to a simple trace constituent air transport problem. Fate of pollutants in the air and water environments, Part I. *Advances in Environmental Science and Technology*, Vol. 8, I. H. Suffet, Ed., Wiley and Sons, 223–252.

Manton, M. J., and W. R. Cotton, 1977: Formulation of approximate equations for modeling moist deep convection on the mesoscale. Atmos. Sci. Pap. No. 266, Colorado State University, 62 pp.

Marshall, J. S., and W. McK. Palmer, 1948: The distribution of raindrops with size. *J. Meteor.*, **5**, 165–166.

Murray, F. W., and L. R. Koenig, 1972: Numerical experiments on the relation between microphysics and dynamics in cumulus convection. *Mon. Wea. Rev.*, **100**, 717–732.

Ogura, Y., and N. A. Phillips, 1962: Scale analysis of deep and shallow convection in the atmosphere. *J. Atmos. Sci.*, **19**, 173–179.

——, L. Chen, J. Russel and S.-T. Soong, 1979: On the formation of organized convective systems observed over the eastern Atlantic. *Mon. Wea. Rev.*, **107**, 426–441.

Piacsek, S. A., and G. P. Williams, 1970: Conservative properties of convection difference schemes. *J. Comput. Phys.*, **6**, 392–405.

Roll, H. U., 1965: *Physics of the Marine Atmosphere.* Academic Press, 426 pp.

Sommeria, G., 1976: Three-dimensional simulation of turbulent processes in an undisturbed trade wind boundary layer. *J. Atmos. Sci.*, **33**, 216–241.

Soong, S.-T., and Y. Ogura, 1973: A comparison between axisymmetric and slab-symmetric cumulus cloud models. *J. Atmos. Sci.*, **30**, 879–893.

——, and ——, 1980: Response of tradewind cumuli to large-scale processes. *J. Atmos. Sci.*, **37**, 2035–2050.

——, and W.-K. Tao, 1980: Response of deep tropical cumulus clouds to mesoscale processes. *J. Atmos. Sci.*, **37**, 2016–2034.

——, and ——, 1984: A numerical study of the vertical transport of momentum in a tropical rainband. *J. Atmos. Sci.*, **41**, 1049–1061.

Srivastava, R. C., 1978: Parameterization of raindrop size distributions. *J. Atmos. Sci.*, **35**, 108–117.

Tao, W.-K., 1983: A numerical study of the structure and vertical transport properties of a tropical convective system. Ph.D. dissertation, University of Illinois, 228 pp.

Tripoli, G. J., and W. R. Cotton, 1980: A numerical investigation of several factors contributing to the observed variable intensity of deep convection over South Florida. *J. Appl. Meteor.*, **19**, 1037–1063.

Weisman, M. L., and J. B. Klemp, 1982: The dependence of numerically simulated convective storms on vertical wind shear and buoyancy. *Mon. Wea. Rev.*, **110**, 504–520.

Wilhelmson, R. B., and Y. Ogura, 1972: The pressure perturbation and the numerical modeling of a cloud. *J. Atmos. Sci.*, **29**, 1295–1307.

Williams, G. P., 1969: Numerical integration of the three-dimensional Navier–Stokes equations for incompressible flow. *J. Fluid Mech.*, **37**, 727–750.

——, 1972: Friction term formulation and convective instability in a shallow atmosphere. *J. Atmos. Sci.*, **29**, 870–876.

Zipser, E. J., and M. A. LeMone, 1980: Cumulonimbus vertical velocity events in GATE. Part II: Synthesis and model core structure. *J. Atmos. Sci.*, **37**, 2458–2469.

——, R. J. Meitin and M. A. LeMone, 1981: Mesoscale motion fields associated with a slowly moving GATE convective band. *J. Atmos. Sci.*, **38**, 1725–1750.